pH-Activated Nanoparticles for Controlled Topical Delivery of Farnesol To Disrupt Oral Biofilm Virulence

Benjamin Horev,[†,□] Marlise I. Klein,[‡,○,□] Geelsu Hwang,[§] Yong Li,[§] Dongyeop Kim,[§] Hyun Koo,[*,‡,§,∥,@] and Danielle S. W. Benoit[*,†,⊥,#,@]

[†]Department of Biomedical Engineering, [‡]Center for Oral Biology, [⊥]Department of Chemical Engineering, and [#]Center of Musculoskeletal Research, University of Rochester, Rochester, New York 14627, United States and [§]Biofilm Research Lab, Levy Center for Oral Health, and [∥]Department of Orthodontics and Divisions of Pediatric Dentistry and Community Oral Health, School of Dental Medicine, University of Pennsylvania, Philadelphia, Pennsylvania 19104, United States. [○]Present address for M.I.K.: Department of Dental Materials and Prosthodontics, Araraquara Dental School, Universidade Estadual Paulista, UNESP, Sao Paulo, Brazil. [□]B. Horev and M. I. Klein contributed equally to this work. [@]Co-senior authors.

ABSTRACT Development of effective therapies to control oral biofilms is challenging, as topically introduced agents must avoid rapid clearance from biofilm–tooth interfaces while targeting biofilm microenvironments. Additionally, exopolysaccharides-matrix and acidification of biofilm microenvironments are associated with cariogenic (caries-producing) biofilm virulence. Thus, nanoparticle carriers capable of binding to hydroxyapatite (HA), saliva-coated HA (sHA), and exopolysaccharides with enhanced drug release at acidic pH were developed. Nanoparticles are formed from diblock copolymers composed of 2-(dimethylamino)ethyl methacrylate (DMAEMA), butyl methacrylate (BMA), and 2-propylacrylic acid (PAA) (p(DMAEMA)-*b*-p(DMAEMA-*co*-BMA-*co*-PAA)) that self-assemble into ~21 nm cationic nanoparticles. Nanoparticles exhibit outstanding adsorption affinities (~244 L-mmol^{-1}) to negatively charged HA, sHA, and exopolysaccharide-coated sHA due to strong electrostatic interactions *via* multivalent tertiary amines of p(DMAEMA). Owing to hydrophobic cores, nanoparticles load farnesol, a hydrophobic antibacterial drug, at ~22 wt %. Farnesol release is pH-dependent with $t_{1/2}$ = 7 and 15 h for release at pH 4.5 and 7.2, as nanoparticles undergo core destabilization at acidic pH, characteristic of cariogenic biofilm microenvironments. Importantly, topical applications of farnesol-loaded nanoparticles disrupted *Streptococcus mutans* biofilms 4-fold more effectively than free farnesol. Mechanical stability of biofilms treated with drug-loaded nanoparticles was compromised, resulting in >2-fold enhancement in biofilm removal under shear stress compared to free farnesol and controls. Farnesol-loaded nanoparticles effectively attenuated biofilm virulence *in vivo* using a clinically relevant topical treatment regimen (2×/day) in a rodent dental caries disease model. Strikingly, treatment with farnesol-loaded nanoparticles reduced both the number and severity of carious lesions, while free farnesol had no effect. Nanoparticle carriers have great potential to enhance the efficacy of antibiofilm agents through multitargeted binding and pH-responsive drug release due to microenvironmental triggers.

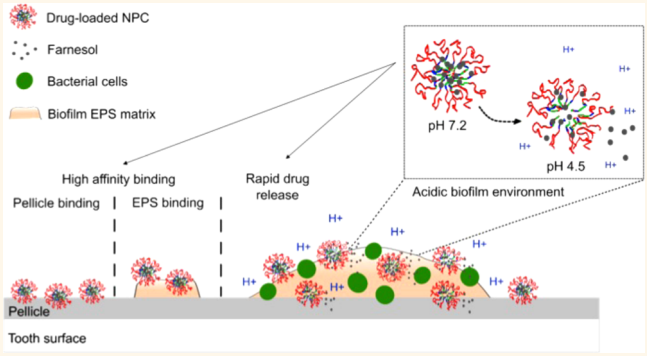

KEYWORDS: polymeric micelles · pH-responsive · nanoparticles · dental pellicle · exopolysaccharides · matrix · dental caries · *Streptococcus mutans* biofilms · farnesol

The majority of persistent infectious diseases in humans are caused by virulent biofilms, including those occurring in the mouth, *e.g.*, dental caries and periodontal disease.[1,2] The annual treatment cost of oral biofilm-related diseases is ~$81 billion in the U.S. alone.[3] Biofilms develop when microbes accumulate on surfaces, forming structured communities encapsulated within an extracellular matrix composed of polymeric substances such as exopolysaccharides (EPS).[2,4,5] In the oral cavity, caries-producing (cariogenic) biofilms assemble on pellicle-covered teeth, as an EPS-rich matrix rapidly develops in the presence of dietary sucrose.[6−9] EPS, produced by bacterial exoenzymes (*e.g.*, glucosyltransferases), promote local accumulation of pathogens (*e.g.*, *Streptococcus mutans*) while forming a diffusion-limiting polymeric matrix that protects the embedded bacteria.[2,4,5] In parallel, sugars are

* Address correspondence to benoit@bme.rochester.edu, koohy@dental.upenn.edu.

Received for review April 28, 2014 and accepted February 8, 2015.

Published online February 09, 2015
10.1021/nn507170s

fermented by bacteria within the EPS matrix, creating highly acidic microenvironments.[7,8,10] In human dental biofilm, also known as plaque, pH values often reach pH ~4.5 or even lower, particularly after exposure to sucrose, starch, and other cariogenic food products.[11−14] At sites of active caries, persistent acidic plaque of pH ~4.5−5.5 can result.[11−14] The low-pH niches induce EPS synthesis, while *S. mutans* and other cariogenic organisms thrive,[15] ensuring continuous biofilm accumulation, acid-dissolution of tooth enamel, and ultimately the onset of carious lesions.[7−10,16] Resident microorganisms become recalcitrant to antimicrobial therapies, stemming from a combination of bacterial drug resistance and reduced drug bioavailability and persistence within biofilm microenvironments.[1,2]

The development of novel therapeutic approaches against oral biofilms is challenging, as topically introduced antibacterial agents are not retained at necessary concentrations for prolonged periods due to rapid clearance by saliva. There exists a need to enhance the bioavailability and retention of antibacterial agents at the dental surfaces and within the biofilm. A fundamental understanding of biofilm matrix assembly and changes in the biofilm microenvironment offers opportunities to exploit drug delivery systems. Several strategies have been developed. These include materials with inherent antimicrobial properties such as cationic liposomes and silver particles,[2,17−20] as well as drug delivery systems with specific affinity to tooth surfaces.[19,21−25] However, these approaches are mostly designed to target hydroxyapatite, the mineral component of tooth enamel, rather than the pellicle, the proteinaceous film that covers hydroxyapatite-based enamel in the mouth, or EPS. None of these strategies exploit the acidic milieus within EPS-rich biofilm microenvironments to trigger drug delivery. Nevertheless, delivery systems have been developed to release drugs or biologically active molecules in response to other acidic environments, such as in tumors, cellular endosomes or lysosomes, or sites of bacterial infections.[20,26−29] These include acid-degradable residues[30,31] and nanoparticles that incorporate pH-responsive residues such as diethylaminoethyl methacrylate (DEAEMA),[32,33] dimethylaminoethyl methacrylate (DMAEMA),[34,35] propylacrylic acid (PAA),[36−38] or combinations thereof[26−29,39] to trigger drug delivery *via* nanoparticle destabilization at low pH.

There exists an opportunity to advance drug delivery approaches for oral biofilms by providing localized drug release at the pellicle/biofilm interface and within an EPS-rich matrix in response to acidic pH niches, where pathogenic (cariogenic) bacteria prosper and actively develop biofilms. To address this challenge, nanoparticles with exciting properties for antibiofilm delivery were developed. We describe pH-activated polymer-based nanoparticles that bind with high affinity to tooth surfaces (hydroxyapatite and pellicle) and EPS, enhancing drug retention at at-risk sites for biofilm development. The nanoparticles contain pH-responsive moieties that expedite drug release at acidic pH values found within cariogenic biofilm microenvironments, resulting in excellent antibiofilm activity and effectively reducing the onset of carious lesions *in vivo*. Specifically, nanoparticles composed of cationic poly(dimethylaminoethyl methacrylate) (p(DMAEMA)) coronas and hydrophobic and pH-responsive p(DMAEMA-*co*-BMA-*co*-PAA) cores[30,36] were used to achieve high affinity, multivalent binding to tooth surfaces and EPS. A hydrophobic antibacterial agent, farnesol, effective against planktonic *S. mutans* cells, but with limited activity against cariogenic biofilms following topical applications,[43] was used to demonstrate enhanced drug efficacy through high-capacity nanoparticle-mediated delivery. Altogether, we show that the developed nanoparticle composition and formulation exhibits outstanding binding affinities to pellicle and EPS surfaces (~244 L-mmol^{-1}) as well as drug loading capacities (up to ~22 wt %) and pH-dependent drug release. Farnesol was released rapidly at acidic pH due to protonation of DMAEMA and PAA residues within nanoparticle cores and resulting destabilization of nanoparticle structure. Topical applications of farnesol-loaded nanoparticles that target and localize high farnesol depots on surfaces and within the EPS matrix disrupted *S. mutans* biofilms 4-fold more effectively than free farnesol. The mechanical stability of treated biofilms was compromised, resulting in >2-fold enhancement in biofilm removal from pellicle-coated apatitic surfaces upon exposure to shear stress, compared to free farnesol treatments or to controls. Ultimately, the efficacy of nanoparticle-mediated drug delivery on biofilm virulence was demonstrated through reductions in both the incidence and the severity of carious lesions *in vivo*, using a clinically relevant twice-daily topical treatment regimen. The achieved drug retention and subsequent *in vivo* therapeutic effect of topically applied nanoparticles are highly desirable properties for the development of novel and efficacious therapies for biofilm-related oral diseases such as dental caries.[6]

RESULTS AND DISCUSSION

Polymer Structure and Function. All polymers used in this work were synthesized *via* reversible addition−fragmentation chain transfer (RAFT) polymerizations, which provide precise control over polymer molecular weights and polydispersity indices (M_w/M_n, PDI < 1.3). The structure, composition, and physical properties of pH-responsive p(DMAEMA)-*b*-p(DMAEMA-*co*-BMA-*co*-PAA) that form micelle-based nanoparticles and of polymers used as controls for adsorption to pellicle and EPS surfaces are detailed in Table 1 and Figure 1. p(DMAEMA)-*b*-p(DMAEMA-*co*-BMA-*co*-PAA) diblocks were synthesized in a two-step RAFT polymerization

TABLE 1. Characterization of All Polymers and Micelle-Base Nanoparticles Employed in Binding Experiments[a]

polymers									micelles		
corona blocks					core blocks	diblock copolymers					
abbreviation	composition	MW	PDI	DP	composition	MW	PDI	DP	size (*d*, nm)	size PDI	ζ (mV)
NPC	p(DMAEMA)	12.1 kDa	1.3	100	p(DMAEMA-*co*-BMA-*co*-PAA)	24.1 kDa	1.1	175	21 ± 0.4	0.2 ± 0.09	+16 ± 1.3
C1	p(DMAEMA)	16.2 kDa	1.01	100	NA	NA	NA	NA	ND (soluble)	ND	ND
C2	p(PEGMA)	20.2 kDa	1.08	100	p(DMAEMA-*co*-BMA-*co*-PAA)	31.6 kDa	1.09	250	21 ± 0.9	0.37 ± 0.05	−1.6 ± 0.7
C3	p(DMAEMA)	24.6 kDa	1.08	150	p(BMA)	37.4 kDa	1.01	250	38 ± 2.8	0.21 ± 0.02	+17 ± 1.7

[a] MW is weight average molecular weight, PDI is the molecular weight polydispersity index, DP is degree of polymerization, size PDI is the polydispersity of micelle diameters, and ζ is micelle zeta-potential. Nanoparticle sizes and zeta-potentials were measured at pH 7.2. NA not applicable (no micelle structure), and ND not detectable.

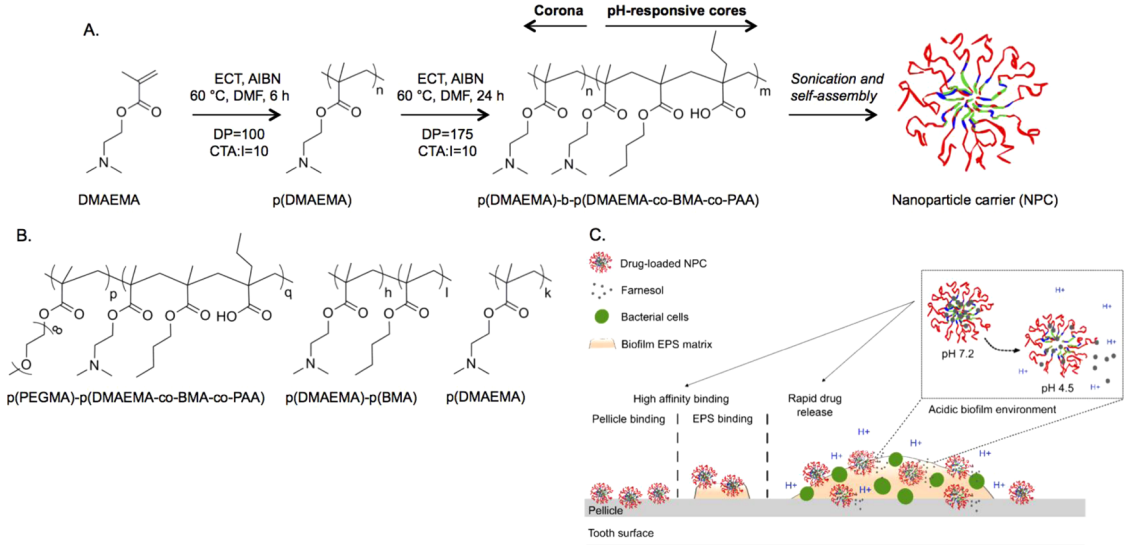

Figure 1. Structure and function of nanoparticles and properties of used polymers. (A) Depiction of the chemistry and self-assembly of diblock copolymers. Cationic and pH-responsive ~20 kDa diblock copolymers with equivalent first- to second-block molecular weights and PDI of 1.1 were synthesized by two-step RAFT polymerizations, as indicated, and self-assembled into micelle-based nanoparticles in aqueous solutions *via* sonication. (B) Structures of control polymers utilized to isolate required physicochemical characteristics for binding to dental surfaces. (C) Proposed mode of action of pH-responsive nanoparticles for prevention and/or treatment of biofilms. RAFT is reversible addition−fragmentation chain transfer polymerization. PDI is polydispersity index; ECT is the chain transfer agent (CTA), 4-cyano-4-[(ethylsulfanylthiocarbonyl-)sulfanyl]pentanoic acid; AIBN is the initiator, 2,2-azobis(isobutyronitrile); DMF is dimethylformamide; DP is degree of polymerization.

with equivalent first- to second-block molecular weights (Table 1 and Figure 1A). First, positively charged 9.3 kDa p(DMAEMA) blocks were synthesized (PDI = 1.3) (Table 1 and Figure 1A). From this p(DMAEMA) macro-chain-transfer agent (CTA), second pH-responsive p(DMAEMA-*co*-BMA-*co*-PAA) blocks were added[26,28,29] (Figure 1A and Table 1), so that the overall molecular weight of the nanoparticle-forming polymer was 21.9 kDa (PDI = 1.1). Control block copolymers that form polymeric micelle-based nanoparticles were synthesized similarly (Figure 1B and Table 1). p(PEGMA)-*b*-p(DMAEMA-*co*-BMA-*co*-PAA) polymers (Table 1, C2) were synthesized with 18.7 kDa (PDI = 1.08) and 29.0 kDa (PDI = 1.09) first block and overall molecular weights, respectively (Table 1), whereas p(DMAEMA)-*b*-p(BMA) polymers (Table 1, C3) were synthesized with 22.8 kDa (PDI = 1.08) first-block and 37 kDa (PDI = 1.01) overall molecular weights. Note that tercopolymer blocks were composed of ~25:50:25% DMAEMA:BMA:PAA monomers, as analyzed *via* proton nuclear magnetic resonance spectroscopy.

Polymer diblocks form micelles due to solution thermodynamics. Cationic p(DMAEMA) coronas interact favorably with aqueous media, while hydrophobic and pH-responsive p(DMAEMA-*co*-BMA-*co*-PAA) cores do not and become sequestered into the interior of micelles.[26,28,29,40] p(DMAEMA)-*b*-p(DMAEMA-*co*-BMA-*co*-PAA) diblocks self-assemble into ~21 nm, monodisperse micelles (size PDI = 0.2) (Table 1) with low critical micelle concentrations (CMC) (0.008 mg/mL, Supplemental Figure S1). The CMC measured for the

micelle-based nanoparticles was comparable to reported values (0.002 mg/mL) for diblocks with similar polymer compositions;[41] therefore nanoparticles are stable down to micromolar concentration ranges for drug delivery applications. Liposomal or detergent-based micelles are typically less stable, limiting their utility as drug carriers.[42] As p(DMAEMA) is 50% protonated at physiologic pH owing to tertiary amine residues (pK_a ~7.5), nanoparticle surface potentials (ζ-potentials) are positive ($\zeta = +16$ mV) (Table 1).[43,44] Therefore, nanoparticles can be employed for multivalent-targeted drug delivery to negatively charged sites on pellicle and EPS surfaces.

Control polymers, including p(DMAEMA) (C1), and diblocks of p(PEGMA)-*b*-p(DMAEMA-*co*-BMA-*co*-PAA) (C2) and p(DMAEMA)-*b*-p(BMA) (C3) were used to demonstrate the role of p(DMAEMA) coronas and nanoparticle structures in binding to pellicle and EPS surfaces (Figure 1B). Nanoparticles with either neutral or positive ζ-potentials were used (Table 1). For example, 21 nm (diameter, size PDI = 0.37) nanoparticles with p(PEGMA) coronas and pH-responsive cores (C2) have slightly negative ζ-potentials ($\zeta = -1.6$ mV) (Table 1, comparable to ~0 mV ζ-potentials reported for nanoparticles with p(PEGMA) coronas[20,32]) and were used to demonstrate surface charge-dependent binding. Alternatively, 38 nm micelles (diameter, size PDI = 0.21) with p(DMAEMA) coronas and p(BMA) cores (C3) that lack pH-responsive PAA and DMAEMA residues within micelle cores and have similar ζ-potentials ($\zeta = +17$ mV) to nanoparticles (Table 1) were used to demonstrate that surface charge and not pH-responsive moieties within the nanoparticle cores mediate binding to dental surfaces. In addition, 16.0 kDa p(DMAEMA) (PDI = 1.01) was used as a positive control of electrostatic binding of polymers at pH 7.2 when 50% of p(DMAEMA) amine residues are protonated (pK_a ~7.5)[43,44] and as a negative control at pH 10.5, when the amine residues are completely deprotonated. p(DMAEMA) alone did not form nanoparticles; therefore diameters, PDI, and ζ-potentials for p(DMAEMA) were not measurable (Table 1).

Nanoparticle Binding to "at-Risk" Surfaces for Biofilm Development. *Mechanisms of Nanoparticle Binding to Pellicle and EPS Surfaces.* Effective drug-loaded micelle binding to "at-risk" surfaces is critical to increase retention and antibacterial drug concentrations *in situ*. Additionally, acidic pH within biofilm environments (pH ≈ 4.5−5.5)[7,8,10] can be exploited for improved binding, micelle destabilization, and pH-triggered drug release. Surface binding depends on several factors, including polymer size and charge density, pH, and ionic strength.[45,46] Proteins of tooth-pellicle or carbohydrates/glycosyl linkages of bacterially derived EPS can provide specific binding to biomolecules.[4,47−49] Generally, adsorption of amines to hydroxyapatite is mediated through protonated residues that electrostatically interact with OH^- and the PO_4^- groups of hydroxyapatite (HA) or through PO_4^- bridges with Ca^{2+} ions on HA surfaces.[50] It is well established that cationic moieties bind to negatively charged sites of pellicle, bacterial membranes, and biofilm surfaces.[2,20,51−56] Thus, three distinct surfaces were used to characterize polymer binding mechanisms as well as quantify binding capacities and affinities (Figure 2): uncoated HA that mimics tooth mineral or dental enamel; HA coated with saliva (sHA) that mimics tooth-enamel pellicle;[47,54,57] and Gtf-derived EPS (glucans)-coated sHA (gsHA) that emulates EPS, as Gtf-derived glucans are the primary exopolysaccharides produced on tooth-pellicle and are one of the main constituents of the extracellular matrix of cariogenic biofilms.[4,49] Importantly, as glucans are synthesized *in situ* by pellicle-adsorbed Gtfs, gsHA surfaces closely resemble the structural organization and the topography of intact EPS, which are critical for exploration of nanoparticle binding properties.

As shown in Figure 2A, 67%, 60%, and 44% of nanoparticles bound to HA, sHA, and gsHA, respectively, as compared to 70%, 76%, and 79% of p(DMAEMA) at pH 7.2. These data indicate that tertiary amine residues of p(DMAEMA) coronas, as they are 50% protonated at physiologic pH,[43,44] provide binding capability to nanoparticles (and micelles with alternative cores) to negatively charged sites of dental surfaces.[2,53,54,56] The decrease in nanoparticle binding to sHA and gsHA relative to p(DMAEMA) at pH 7.2 is likely a result of screening of the HA surface by salivary components within the sHA and glucans on gsHA surfaces and possibly due to more thermodynamically favorable assembly of p(DMAEMA) polymers with pellicle proteins or glucans, compared to the 21 nm nanoparticle assemblies. Phosphate- and alendronate-functionalized pluronic-based micelles have been previously explored for localized release of antibacterial drugs. These structures exhibit 50% and 35% binding to HA.[21,23] Overall, these values are lower than nanoparticle binding to HA, likely due to more modest valency of functionalities responsible for binding, as the corona of the nanoparticles are exclusively formed from cationic DMAEMA, while only one functionality (at maximum) is present within the pluronic chains composing the micelles.

The role of p(DMAEMA) amine protonation in micelle targeting was confirmed when, as compared to p(DMAEMA) at pH 7.2, deprotonated p(DMAEMA) (at pH 10.5) did not bind to HA (0.5%) and bound much less prominently to sHA (25.9%) and gsHA (36.2%) (Figure 2A). The observation of detectable adsorption of deprotonated p(DMAEMA) (at pH 10.5) to sHA and gsHA surfaces also supports alternative binding mechanisms (*e.g.*, binding to pellicle proteins or glucans possibly through H-bonding and hydrophobic interactions).

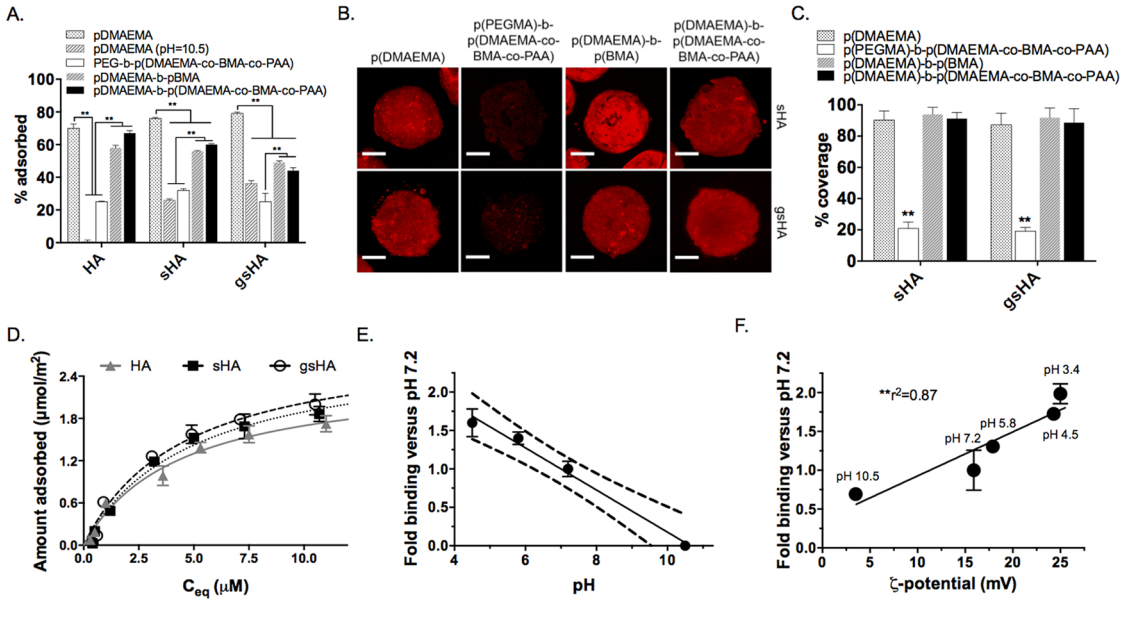

G.

Surface	b_{max} (μmol/m^2)	K_a (L-mmol^{-1})
HA	2.4±0.2	230±52
sHA	2.8±0.2	228±25
gsHA	2.9±0.3	273±42

Figure 2. Characterization of nanoparticle binding to dental surfaces. (A) Characterization of polymer binding through cationic p(DMAEMA) coronas, performed at 1 μM and at pH 7.2. The error bars represent standard error (n = 3 independent experiments), and the asterisks denote significant differences at $p < 0.01$. (B) Confocal images of polymer binding at 85 μM and pH 7.2 (scale bars, 20 μm) and (C) percent surface area covered by polymers. Nanoparticles with PEG coronas bound to a much lower extent compared to nanoparticles with p(DMAEMA) coronas and to p(DMAEMA) alone. The error bars represent standard deviation (n = 3 independent experiments), and the asterisks denote significant differences at $p < 0.01$. (D) Equilibrium binding profile of nanoparticles at increasing polymer concentrations. The solid and dotted lines represent Langmuir fits to the adsorption data (SE, n = 3 independent experiments, df = 18). (E) Fold increases in binding of p(DMAEMA) to hydroxyapatite (HA), as a function of pH. (F) Fold increase in nanoparticle binding as a function of ζ-potential at a range of pH values. Binding and ζ-potential were altered by varying the pH of nanoparticle solutions, as indicated on the graph. The binding of p(DMAEMA) and nanoparticles to HA was similar and increased as pH decreased ($R^2 > 0$), as assessed by two-tailed t tests on Pearson correlations ($p < 0.01$). For E and F, the error bars represent SEM (n = 3 independent experiments), the solid lines denote Pearson correlation, and external and internal dotted lines denote confidence intervals of Pearson correlation at 95% confidence. (G) Langmuir fit parameters that define binding capacity (b_{max}) and binding affinity (K_a). The Langmuir equation parameters were calculated based on data presented in D ($R^2 > 0.98$). HA, uncoated hydroxyapatite; sHA, saliva-coated HA; gsHA, glucans-coated sHA.

To further establish the role of p(DMAEMA) coronas in nanoparticle targeting to each of the dental surfaces and to assess whether pH-responsive cores of nanoparticles impact binding, nanoparticle adsorption was compared to polymers that also form nanoparticles (C2 and C3) (Figure 2A, Figure 1B). These included nanoparticles formed from block copolymers of p(DMAEMA)-*b*-p(BMA) and p(PEGMA)-*b*-(DMAEMA-*co*-BMA-PAA) (Figure 1B). p(DMAEMA)-p(BMA) were utilized to confirm the role of p(DMAEMA) coronas and not pH-responsive nanoparticle cores in binding, whereas p(PEGMA)-*b*-(DMAEMA-*co*-BMA-PAA) micelles were used as a nontargeting control, as substitution of p(DMAEMA) with p(PEGMA) coronas resulted in neutral micelle surface potentials (Table 1). p(DMAEMA)-*b*-p(BMA) polymers binding to each of the surfaces (HA (58%), sHA (56%), gsHA (49%)) was similar to that of nanoparticles (Figure 2A). Finally, adsorption of nanoparticles relative to polymers with charge neutral (Table 1) p(PEGMA) coronas and pH-responsive p(DMAEMA-*co*-BMA-*co*-PAA) cores was assessed to confirm that nanoparticles require p(DMAEMA) coronas for binding. p(PEGMA)-*b*-p(DMAEMA-*co*-BMA-*co*-PAA) nanoparticles bound poorly to uncoated and pellicle or EPS-coated HA surfaces (25%, 32%, 25%) (Figure 2A), likely as a result of minimal electrostatic interactions of neutral p(PEGMA) coronas ($\zeta = -1.6$ mV) with these surfaces compared to protonated p(DMAEMA) coronas of nanoparticles ($\zeta = +16$ mV).

Binding of polymers to pellicle and EPS surfaces was confirmed by confocal imaging (Figure 2B). Similar to the quantitative data, confocal images show that binding of nanoparticles, p(DMAEMA)-*b*-p(BMA), and p(DMAEMA) was greater than binding of nanoparticles with p(PEGMA) coronas to both sHA and gsHA surfaces. Likewise, the following polymer surface coverage for sHA and gsHA was observed: 21% and 19% by

p(PEGMA)-*b*-p(DMAEMA-*co*-BMA-*co*-PAA) as compared to 90% and 87% by p(DMAEMA), 94% and 92% by p(DMAEMA)-*b*-p(BMA), and 91% and 89% by nanoparticles, as shown in Figure 2C. Overall, we show that the mechanism of nanoparticle binding to HA, sHA, and gsHA is mediated primarily through cationic coronas of nanoparticles and that nanoparticles with positive surface potentials are preferable for binding to pellicle and EPS surfaces. These observations are similar to cationic, histidine-functionalized particles.[20] In addition, pH-responsive components within nanoparticle cores do not impact nanoparticle surface potentials or their binding properties.

Binding Affinity and Capacity of Nanoparticles for Hydroxyapatite, Pellicle, and EPS Surfaces. More sophisticated adsorption experiments were performed using nanoparticles composed of p(DMAEMA)-*b*-p(DMAEMA-*co*-BMA-*co*-PAA) (Figure 2D), as these micelles exhibited the greatest adsorption characteristics and also have inherent pH-responsive behaviors.[26,28,29] According to Langmuir fits to adsorption data (Figure 2G), the average maximal binding capacity (b_{max}) of nanoparticles on mimetic surfaces was ~2.7 μmol/m^2 and the adsorption affinity constants (K_a) were ~244 L-mmol^{-1}. These values did not differ statistically among the tested surfaces. The affinity of nanoparticle binding was found to be several orders of magnitude higher than the affinity of several bisphosphonates (BPs) to hydroxyapatite. Adsorption capacities of BP[58−62] were comparable to those of nanoparticles, which implies that nanoparticles bind more rapidly, a characteristic important for topical treatments, but at comparable maximal amounts to BP. The reported b_{max} and K_a of BPs, which are known to have exceptionally high affinity to hydroxyapatite, are within the range 2.17−2.31 μmol/m^2 and 1−3470 L-mmol^{-1},[58−64] similar to the characteristics of the nanoparticles described herein. The use of p(DMAEMA) polymers for targeting of negatively charged surfaces, reported here for the first time, may find use in other applications requiring HA binding capabilities.

Remarkably, the affinities of nanoparticles to HA, sHA, and gsHA (Figure 2G) are greater than several types of nanoparticles functionalized with alendronate, a bisphosphonate, and peptides engineered for favorable binding to HA ($K_a \approx$ 18.4−70.9 L-mmol^{-1}).[65] Uncoated HA rarely, if ever, occurs in the oral cavity, as *in vivo,* teeth are covered by a proteinaceous salivary film known as pellicle. The binding/targeting mechanisms of nanoparticles for HA are important to understand and to allow for comparisons to previous work measured primarily with unaltered hydroxyapatite surfaces. It is clear that nanoparticles bind equally well to more clinically relevant sHA- and EPS-coated (gsHA) surfaces.

pH-Dependent Binding of Nanoparticles. The impact of acidic pH on nanoparticle surface potentials and targeting properties was investigated, as biofilm microenvironments may reach a pH of ~4.5−5.5,[7,8,10] and this property can be exploited to improve nanoparticle binding. For simplicity, pH-responsive, amine protonation-dependent binding of p(DMAEMA) was examined on hydroxyapatite surfaces. Binding of p(DMAEMA) at acidic pH was stronger (Figure 2E) compared to physiological conditions due to increased protonation of amine residues. Thus, DMAEMA is suitable for targeted drug delivery to negatively charged surfaces at pathological (cariogenic) conditions, which results in localized acidic pH.[8] Similar to p(DMAEMA), binding of nanoparticles increased at low pH (Figure 2F). When binding is performed at pH 10.5, conditions at which amines of p(DMAEMA) coronas are deprotonated, ~70% of nanoparticles became bound compared to nanoparticle binding observed at pH 7.2. In comparison to nanoparticles, 0% of p(DMAEMA) bound at pH 10.5 (Figure 2E), similar to data presented in Figure 2A. This suggests that other factors may also affect the binding of nanoparticles to apatitic surfaces. These factors may include nanoparticle excluded volume interactions that are increased with nanoparticle diameter and multivalency of amine residues within the nanoparticle coronas,[50] both of which could result in different interactions with dental surfaces.

pH-responsive nanoparticle binding was further investigated through additional analysis of binding as a function of nanoparticle ζ-potential (Figure 2F). As shown in Figure 2F, nanoparticle binding correlates with ζ-potential, which was altered by changing nanoparticle solution pH (Supplemental Figure S2), as previously described.[20,32] A significant positive correlation between nanoparticle binding and ζ-potential was observed (Figure 2F). Greater binding and higher ζ-potentials of nanoparticles at acidic pH (Figure 2E,F) likely relate to increased protonation of amines of p(DMAEMA), similar to studies with histidine-functionalized nanoparticles,[20] which could also contribute to nanoparticle interactions with negatively charged tooth surfaces, EPS, and bacterial surfaces.[20,50]

Drug Loading Capacity of Nanoparticles. p(DMAEMA)-*b*-p(DMAMEA-*co*-BMA-*co*-PAA) nanoparticles were shown to bind to hydroxyapatite and to surfaces on which biofilm forms and accumulates (the pellicle and EPS surfaces). Furthermore, nanoparticles can bind to the EPS matrix of intact *S. mutans* biofilms, as shown by confocal imaging of nanoparticle-treated biofilms (Supplemental Figure S2). Therefore, nanoparticles were further investigated for drug encapsulation. Farnesol was selected to evaluate the potential of nanoparticle-mediated delivery, as farnesol is a hydrophobic antibacterial agent that is highly effective in disrupting the viability and virulence (*i.e.*, acidogenicity and EPS synthesis) of planktonic *S. mutans* but has limited antibiofilm efficacy.[66,67]

Nanoparticles were capable of farnesol loading at up to 22 wt % with loading efficiencies of up to 100%

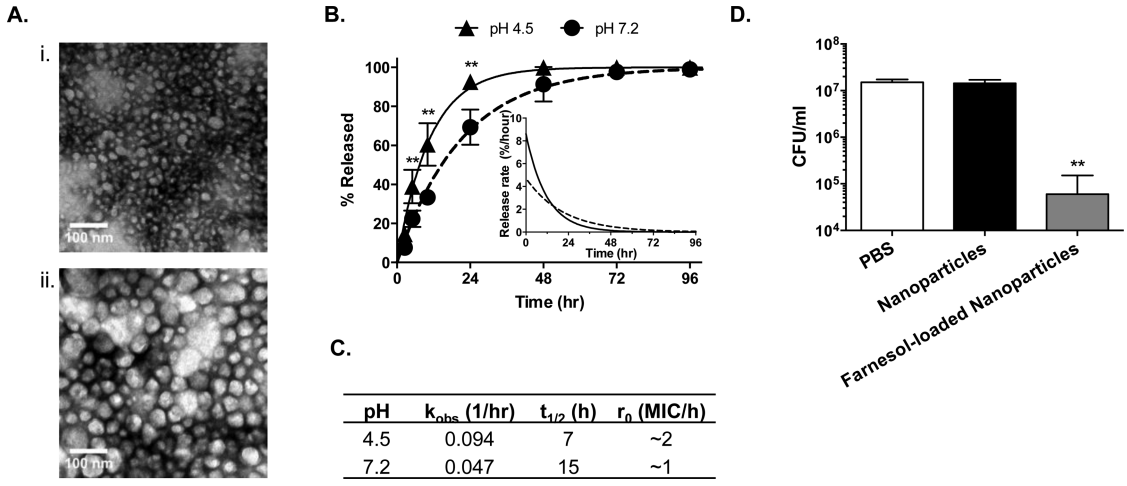

C.

pH	k_{obs} (1/hr)	$t_{1/2}$ (h)	r_0 (MIC/h)
4.5	0.094	7	~2
7.2	0.047	15	~1

Figure 3. Drug loading, pH-responsive release, and antibacterial activity of farnesol-loaded nanoparticles. (A) Transmission electron microscopy (TEM) images that demonstrate an increase in nanoparticle size upon loading; control (unloaded (i) and loaded with farnesol at 21 wt % (ii)). (B) Farnesol release profiles at pH 7.2 and 4.5, including farnesol release rates (inset). Solid and dotted lines show fits ($R^2 > 0.98$) to first-order drug release and release rates determined by first derivative of the fits (inset). (C) Kinetic parameters of release determined from fits to first-order release ($R^2 > 0.98$). Initial release rate (B, inset, r_0), release rate constant (k_{obs}), and half-time of release ($t_{1/2}$) at pH 4.5 suggest 2-fold faster release at pH 4.5 as compared to pH pH 7.2. (D) Antibacterial activity of farnesol-loaded nanoparticles at pH 7.2. A ~2.4 log decrease in bacterial viability was observed after 1 h of exposure to drug-loaded nanoparticles. Error bars represent standard deviation ($n = 3$ independent experiments) for drug release experiments and standard error ($n = 7$) for antibacterial activity experiments. Asterisks denote significant differences at $p < 0.01$, as determined by two-way ANOVA followed by Tukey's test for multiple comparisons.

(Supplemental Figure S3). To our knowledge, the observation that p(DMAEMA)-*b*-p(DMAEMA-*co*-BMA-*co*-PAA) micelles can encapsulate and deliver small-molecule drugs, such as farnesol, has not been reported previously. Even more compelling is that farnesol loading is at ~20-fold higher amounts than its minimum inhibitory concentration (MIC) (~0.014 mg/mL) for *S. mutans*.[68] The concentration of farnesol within nanoparticles is ~440 times higher than its estimated aqueous solubility limit (~1.7 μg/mL). In contrast, a pluronic-based micelle exhibits farnesol loading of 1% or less, possibly due to less robust particle stability consistent with detergent-based micelles or less favorable core−drug interactions.[42] Upon loading at 22 wt %, the size of nanoparticles increased from 21 to 60 nm (Supplemental Figure S4), whereas loading efficiencies were above ~90% throughout the range of investigated loading capacities and the capacity used for biofilm treatments (15 wt %) (Supplemental Figure S3). The spherical shape of nanoparticles and size increases were confirmed by transmission electron microscopy (TEM) for unloaded controls and nanoparticles loaded with farnesol at 22 wt % (Figure 3A). Similar effects on nanoparticle size due to drug loading were reported for micelles formed of poly(lactic-*co*-glycolic acid)-*b*-poly(ethylene glycol) (PLGA-*b*-PEG), poly(styrene)-*b*-poly(ethylene glycol) (PS-*b*-PEG),[69] p(DMAEMA)-p-(BMA),[27] and also pluronics loaded with farnesol.[22] Interestingly, the increase in nanoparticle diameter calculated from specific volumes of farnesol-loaded nanoparticles at 15 wt % is ~16.8 nm, which is similar to the measured increase of ~16.5 nm. The observed increase in nanoparticle size is likely due to assembly and hydrophobic interactions of farnesol with hydrophobic residues of nanoparticle cores or formation of a farnesol phase within the cores, which effectively increases the overall nanoparticle volume.

pH-Triggered Farnesol Release of Nanoparticles. Ideally, nanoparticle-based drug delivery systems would bind to pellicle and EPS surfaces at physiological pH and rapidly release bioactive agents when the environment becomes acidic. The pH within cariogenic biofilms can drop to pH 4.5−5.5 or even lower and persist at low pH values if not effectively neutralized by saliva due to frequent intake of fermentable carbohydrates and the presence of diffusion-limiting EPS matrix. Acidic plaque pH upon sugar exposure is particularly apparent in active caries sites within the mouth.[5,6,8−13,15] Therefore, acidic microenvironments employed as a trigger for micelle destabilization and rapid drug release *in situ* may be a highly efficient approach. Farnesol release from nanoparticles as a function of pH is shown in Figure 3B. Drug release profiles were determined at sink conditions to emulate the *in vivo* environment where continuous drug losses will occur due to repetitively cleared saliva. Farnesol release was pH-dependent, with release rates twice as fast at pH 4.5 compared to pH 7.2 based on first-order release fits (Figure 3B). According to the fits, farnesol release half-life was $t_{1/2}$ = 7 h and $t_{1/2}$ = 15 h for release at pH 4.5 and pH 7.2, respectively. Farnesol release rate over time was modeled, and the resulting predictions are shown in Figure 3B (inset). At pH 4.5, nanoparticles release an amount of drug equivalent to ~1 MIC within ~30 min as compared to ~1 h at

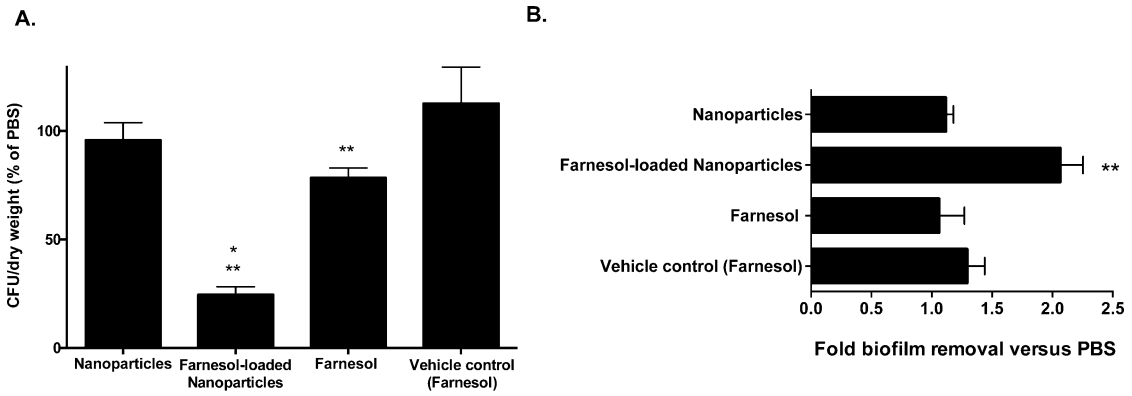

Figure 4. Antibiofilm effects of farnesol delivery *via* nanoparticles. (A) An 80% reduction in the number of colony-forming units per dry weight and (B) a 2-fold increase in biofilm removal under shear stress of 0.184 N/m^2 were achieved in biofilms treated with farnesol-loaded nanoparticles (15 wt %) as compared to controls. Error bars represent standard error, and asterisks denote significant difference (: compared to PBS, nanoparticles, and the vehicle control for farnesol (ethanol); *: compared to farnesol) as assessed by two-way ANOVA followed by Tukey's test for multiple comparisons (n = 4 independent replicates for A and n = 12 independent replicates for B, $p < 0.01$).**

pH 7.2 (Figure 3C and B inset). Furthermore, nearly all drug (~75%) is released at pH 4.5 within ~12 h, whereas complete release at pH 7.2 requires ~30 h. Conversely, the release of the antibacterial drugs triclosan and farnesol from pluronic-based micelles is much slower, releasing only 30% and 20%, respectively, over 2 days at physiological pH. Thus, the overall drug concentrations accessible by these approaches may be more limited than the nanoparticles described here.[22,23] pH-dependent drug release from nanoparticles showed similar trends in buffer that emulates the ionic composition of saliva (Supplemental Figure S5). Importantly, farnesol encapsulated within nanoparticles is biologically active (Figure 3D), showing antibacterial activity against planktonic cells of *S. mutans* after 1 h of exposure to farnesol-loaded nanoparticles (Figure 3D). Additionally, nanoparticles alone did not exhibit any antibacterial activity.

Rapid drug release rates at pH 4.5 are likely due to the pH-responsive behavior of nanoparticle cores.[26,28,29] Specifically, at low pH (4.5), DMAEMA residues (pK_a ~7.2) are fully protonated as compared to ~50% protonation at pH 7.2, whereas PAA residues are neutral.[43,44] The overall cationic charge of the core results in electrostatic repulsion upon DMAEMA protonation at acidic pH, which destabilizes nanoparticle cores and overall micelle structures[26,28,29] (see also Supplemental Figure S6) and thereby triggers farnesol release. Similar pH-dependent drug release from micelles has been described for other pH-dependent moieties, including carboxylic acids.[70] pH-dependent, nanoparticle-mediated release of bioactive farnesol is highly desirable, as nanoparticles bind with high affinity to "at-risk" sites for biofilm formation and rapidly release drug at acidic pH, consistent with actively developing cariogenic biofilms.

Antibiofilm Effects of Farnesol Delivery via Nanoparticles in Situ. Upon establishing high binding affinities to pellicle and EPS surfaces as well as pH-responsive drug release properties of nanoparticles, the impact of nanoparticle-delivered farnesol against *S. mutans* biofilms was explored using an *in vitro* saliva-coated hydroxyapatite biofilm model. Farnesol-loaded nanoparticles (or free farnesol) were applied topically 2 or 3 times per day (a total of 5 applications over 44 h) (see Supplemental Figure S7), emulating clinically relevant dental treatment regimens.[6,66,67,71] Farnesol was encapsulated within nanoparticles at 20-fold higher concentrations (15 wt %) than its minimum inhibitory concentrations for *S. mutans* (~0.014 mg/mL).[68] Equivalent farnesol concentrations were used for free-drug treatment solution, which was solubilized in 15% ethanol (vehicle) due to its poor aqueous solubility. In addition, free nanoparticles or 15% ethanol was used as negative control. We observed a significant, ~80% decrease in colony forming units (CFUs) per biofilm dry weight in the farnesol-loaded nanoparticle treated group (Figure 4A). In sharp contrast, only a modest ~20% decrease in *S. mutans* viability within biofilms was observed when treated with free farnesol (Figure 4A). This effect is consistent with previous reports suggesting insufficient free farnesol retention following topical applications to exert antibiofilm activity *in vitro* and *in vivo*.[66,67] The enhanced antibiofilm activity of farnesol-loaded nanoparticles is likely achieved through nanoparticle-mediated drug delivery, which drastically enhances farnesol retention and bioavailability through drug localization at the pellicle–biofilm interface as well as within the EPS matrix and pH-triggered drug release.

The antibacterial effect observed may also be associated with electrostatic interactions of drug-loaded nanoparticles with bacteria, as cationic nanoparticles are known to bind negatively charged microbial surfaces, including *S. mutans*[2,19,20,53–55] and other biological membranes.[26,28,29] Although free nanoparticles are devoid of antibacterial activity against *S. mutans*,

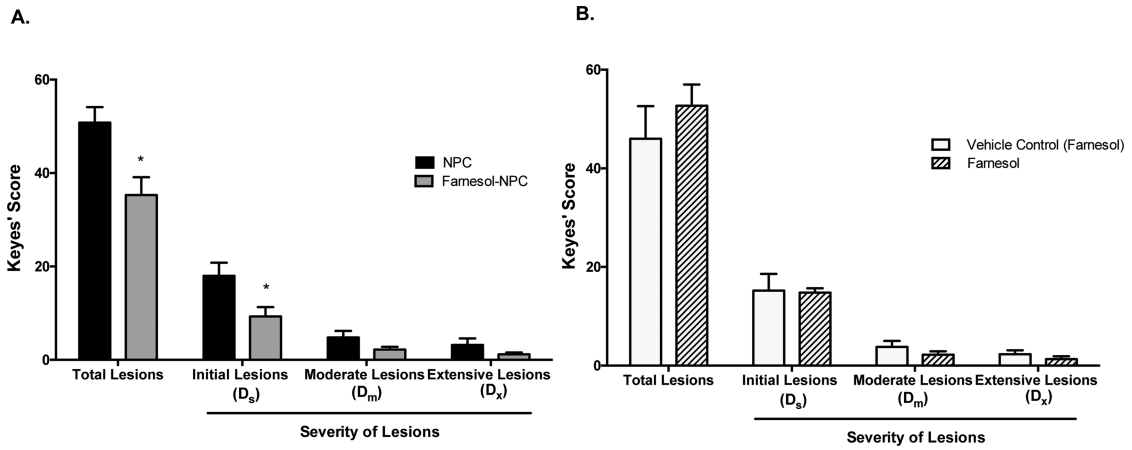

Figure 5. *In vivo* **efficacy assessment of farnesol-loaded nanoparticles (A) and free farnesol (B). Caries scores are presented as mean values with standard error of measurements (n = 6 speciments per experimental condition). Scores are recorded as stages of carious lesion severity according to Larson's modification of Keyes' scoring system: Ds, initial lesion (surface enamel white, broken, and/or dry); Dm, moderate lesion (dentin exposed); Dx, extensive lesion (dentin soft or missing). The nonparametric Mann−Whitney test ($p < 0.05$) was used to assess for treatment efficacy and revealed significant differences between nanoparticles and farnesol-loaded nanoparticle treatments in Total Lesions and Initial Lesions ($p < 0.05$).**

either in planktonic phase or in biofilms (Figure 4), nanoparticle-mediated delivery may facilitate farnesol incorporation into bacterial membranes due to localized release. Whether nanoparticles enhance the ability of farnesol to disrupt membrane integrity[26,28,29,66,68,72] or increase intracellular drug accumulation[73] awaits further mechanistic investigations.

Alternative antibacterial delivery approaches that employ alendronate or phosphate-functionalized pluronic micelles loaded with triclosan or farnesol have shown antibiofilm activity against *S. mutans*.[21−23] However, the targeting of these delivery systems was assessed only on hydroxyapatite surfaces, and delivery efficacy was evaluated after pretreatment of the hydroxyapatite or with continuous, prolonged exposure of established biofilms with drug-loaded micelles, rather than periodic, topical treatment regimens employed herein, precluding direct comparisons between studies. Additionally, none of these previously developed delivery systems take advantage of the acidic biofilm milieu to trigger drug release.

Effective antibiofilm drug delivery systems should also compromise biofilm physical integrity and facilitate biofilm removal through detachment from tooth surfaces. Cariogenic biofilms are particularly difficult to remove, as EPS (*e.g.*, insoluble glucans) interconnects bacterial cells and strengthens their adhesion to apatitic surfaces, forming a highly stable and cohesive biofilms.[9,74,75] Farnesol has shown to moderately reduce EPS production by *S. mutans* within biofilms,[66,67] which could affect biofilm structural integrity. Therefore, the impact of topically applied farnesol-loaded nanoparticles on the mechanical stability of *S. mutans* biofilms was assessed using a shear-inducing device.[75] Biofilms were exposed to a constant shear stress of 0.184 N/m^2 for 10 min using a custom-built device that produces shear flow parallel to biofilm surfaces[75] to detach *S. mutans* biofilms from the sHA surface. After application of shear stress, the amount of biofilm removed relative to PBS-treated biofilms was measured (Figure 4B). We observed more than a 2-fold increase in biofilm removal in farnesol-loaded nanoparticle treated samples compared to free nanoparticles or PBS-treated controls, indicating that the mechanical stability was compromised through treatment with farnesol-loaded nanoparticles. In contrast, free farnesol had no effect compared to its vehicle control (15% ethanol) or PBS-treated controls (Figure 4B). Although shear stress employed herein does not mimic the robust forces of dental scaling/sonication or tooth brushing, biofilm removal upon treatment demonstrates the potential of nanoparticle-mediated drug delivery to weaken and destabilize biofilm structures and to promote its mechanical clearance. Altogether, these data are striking evidence that the antibiofilm activity of farnesol is dramatically enhanced *in situ* through nanoparticle-mediated delivery and retention even after short-term topical exposures, which could ultimately impact the onset of carious lesions *in vivo*.

Nanoparticle-Mediated Farnesol Delivery Disrupts Biofilm Virulence in Vivo. The data from nanoparticle characterization *in vitro* reveals excellent farnesol efficacy against *S. mutans* biofilms, likely due to localization on tooth surfaces as well as within biofilms and expedited farnesol release at acidic pH by nanoparticles. To further examine efficacy, nanoparticle functionalities developed herein were tested for attenuation of biofilm virulence (*i.e.*, the ability to produce carious lesions) on tooth surfaces *in vivo*. Topically applied nanoparticles were assessed using a well-established rodent model of dental caries disease[67,71] to account for nanoparticles' exposure to diet, saliva, host-cellular effects, and hydrodynamic

forces that are typically encountered in the mouth. Cariogenic biofilm formation was promoted by *S. mutans* infection and provision of a sucrose-rich diet.[67,71] Specifically, therapeutic effects of drug-loaded nanoparticles were evaluated by measurement of incidence and severity of smooth-surface lesions, following twice-daily topical application of treatments (Figure 5).

The effects of nanoparticle-mediated farnesol delivery on the onset of carious lesions were striking. Both the number and severity of carious lesions (Ds level) were significantly reduced in farnesol-loaded nanoparticle treated animals compared to nanoparticle controls ($p < 0.05$; Figure 5A), indicating that the initiation and progression of the disease were disrupted. In sharp contrast, free farnesol showed no effect on either incidence or severity of lesions compared to vehicle control (Figure 5B). The excellent cariostatic effect of drug-loaded nanoparticles was exerted despite brief topical exposure to treatments twice daily, likely as nanoparticle-mediated delivery of farnesol promotes drug retention and high bioavailability *in vivo* under cariogenic conditions. This provides evidence of antioral biofilm drug delivery system efficacy in a clinically relevant model of caries disease. Nanoparticle-mediated delivery of drugs is a potent therapeutic approach that can be employed and further optimized to control and prevent biofilm-associated oral diseases such as dental caries using topical treatment regimens.

CONCLUSIONS

In this work, an exciting and efficacious *in situ* drug delivery approach was developed to disrupt cariogenic biofilm virulence *in vivo*. Briefly, pH-responsive nanoparticles were designed to bind avidly to pellicle and EPS, enhancing drug retention at sites where biofilms develop. The nanoparticles are tuned to expedite drug release as the local pH becomes acidic, a feature of cariogenic biofilm microenvironments. Farnesol-loaded nanoparticles robustly increase drug aqueous solubility, which could facilitate further formulation development. Collectively, nanoparticle-mediated drug delivery converts farnesol, an antibacterial agent with limited antibiofilm and anticaries effects, into an effective therapy against dental caries disease. Due to the flexibility and ease of preparation, nanoparticle systems can be designed not only for farnesol but also for other antibiofilm drugs with similar solubility/retention issues. The developed nanoparticle-mediated drug delivery approach can be used to deliver existing or novel agents (alone or in combination) for applications beyond the mouth, as matrix and microenvironmental niches hinder drug efficacy in other types of biofilm-related infections.

MATERIALS AND METHODS

Materials. Chemicals and materials were supplied by Sigma-Aldrich unless otherwise specified. Ethylsulfanylthiocarbonyl sulfanylpentanoic acid (ECT) and propylacrylic acid (PAA) were synthesized as described previously.[29,76] 2,2-Azobis-(isobutyronitrile) (AIBN) was recrystallized from methanol. Dimethylaminoethyl methacrylate (DMAEMA) and butyl methacrylate (BMA) were distilled prior to use, and poly(ethylene glycol) monomethyl ether methacrylate was filtered over basic alumina to remove inhibitor.

Polymer Synthesis. Polymers were synthesized by reversible-addition−fragmentation chain transfer polymerizations that provide precise control over polymer molecular weights and polydispersity indices (M_w/M_n, PDI < 1.3). Specifically the following polymers were synthesized: p(DMAEMA)-*b*-p(DMAEMA-*co*-BMA-*co*-PAA), p(DMAEMA), p(DMAEMA)-p(BMA), and p-(PEGMA)-*b*-p(DMAEMA-*co*-BMA-*co*-PAA). RAFT polymerizations were performed in the presence of monomers, AIBN as the initiator, and ECT as chain transfer agent. The specific reaction conditions for each polymer are detailed below.

Synthesis of Poly(dimethylaminoethyl methacrylate), p(DMAEMA). Three grams of dimethylformamide (DMF) (40 wt % monomer) and 2 g of distilled DMAEMA were introduced into reaction vessels. The initial monomer to CTA ratio ($[M]_0:[CTA]_0$) was such that the molecular weights (M_n) were 16.0 kDa for p(DMAEMA) that was used as a control, 9.1 kDa for p(DMAEMA) that was used as macroCTA for synthesis of block copolymers with p(DMAEMA-*co*-BMA-*co*-PAA), and 22.8 kDa for synthesis of block copolymers with p(BMA) (Figure 1C). CTA to initiator ratios ($[CTA]_0:[I]_0$) were 10:1. Reactions were purged with nitrogen for 40 min using a Schlenk line prior to transfer to an oil bath at 60 °C for polymerization ($t = 6$ h). The resulting polymers (p(DMAEMA)) were isolated by precipitation in 30:70 diethyl ether/pentane and centrifugation. p(DMAEMA) polymers was redissolved in acetone and precipitated in pentane three times and dried overnight *in vacuo*.

Synthesis of Poly(ethylene glycol) Monomethyl Ether Methacrylate, p(PEGMA). Two grams of dehibited poly(ethylene glycol) monomethyl ether methacrylate (360 g/mol) was combined with 3 g of DMF and CTA, at an initial monomer to CTA ratio ($[M]_0:[CTA]_0$) of 150. The solution was purged with nitrogen for 40 min and reacted for 6 h at 60 °C. CTA to initiator ratios ($[CTA]_0:[I]_0$) were 10:1. The resulting p(PEGMA) was isolated by precipitation in 30:70 diethyl ether/pentane and centrifugation. p(PEGMA) polymers were redissolved in acetone and subsequently precipitated in pentane three times and dried overnight *in vacuo*.

Synthesis of p(DMAEMA)-*b*-p(DMAEMA-*co*-BMA-*co*-PAA) Block Copolymers. Diblock copolymers of p(DMAEMA)-*b*-p(DMAEMA-*co*-BMA-*co*-PAA) were synthesized using 9.1 kDa p(DMAEMA) macroCTA. The desired stoichiometric quantities of DMAEMA, PAA, and BMA (25:25:50%, respectively) were added to the p(DMAEMA) macroCTA dissolved in DMF (25 wt % monomers, $[M]_0:[CTA]_0 = 250:1$). CTA to initiator ratios ($[CTA]_0:[I]_0$) were 10:1 with AIBN as the initiator. Following the addition of AIBN, the solutions were purged with nitrogen for 40 min and allowed to react at 60 °C for 24 h. The resulting diblock copolymers were isolated by precipitation in 30:70 diethyl ether/pentane and centrifugation. The polymers were then redissolved in acetone, precipitated in pentane three times, and dried overnight *in vacuo*.

Synthesis of p(PEGMA)-*b*-p(DMAEMA-*co*-BMA-*co*-PAA) Block Copolymers. Diblock copolymers of p(PEGMA)-*b*-p(DMAEMA-*co*-BMA-*co*-PAA) were synthesized using 18.7 kDa p(PEGMA) macroCTA. The desired stoichiometric quantities of DMAEMA, PAA, and BMA (25:25:50%, respectively) were added to the p(PEGMA) macroCTA dissolved in DMF (25 wt % monomers) ($[M]_0:[CTA]_0$, 250:1). CTA to initiator ratios ($[CTA]_0:[I]_0$) were 10:1 with AIBN as the initiator. Following the addition of AIBN, the solutions were purged with nitrogen for 40 min and allowed to react at 60 °C for 24 h. The resulting diblock copolymers were isolated by precipitation in 30:70 diethyl ether/pentane and centrifugation.

The polymers were then redissolved in acetone, precipitated in pentane three times, and dried overnight *in vacuo*.

Synthesis of p(DMAEMA)-*b*-p(BMA) Block Copolymers. Diblock copolymers of p(DMAEMA)-*b*-p(BMA) were synthesized using 22.8 kDa p(DMAEMA) macroCTA. The desired stoichiometric quantities of BMA were added to the p(DMAEMA) macroCTA dissolved in DMF (25 wt % monomers) ($[M]_0$:$[CTA]_0$, 250:1). CTA to initiator ratios ($[CTA]_0$:$[I]_0$) were 10:1 with AIBN as the initiator. Following the addition of AIBN, the solutions were purged with nitrogen for 40 min and allowed to react at 60 °C for 24 h. The resulting diblock copolymers were isolated by precipitation in 30:70 diethyl ether/pentane and centrifugation. The polymers were then redissolved in acetone, precipitated in pentane three times, and dried overnight *in vacuo*.

Polymer Labeling. All polymers were labeled with Texas Red sulfonyl chloride (Thermo Scientific, US) through incubation of 0.25 wt % polymer with 2×10^{-4} wt % Texas Red in triethylamine and dimethylformamide solution (1% v/v). Labeled polymers were purified using dialysis against distilled, deionized water (ddH_2O) using 3500 kDa MWCO membranes (Spectra/Por, Spectrum Laboratories, Rancho Dominquez, CA, USA). Dialysis water was changed twice a day for 5 days, and polymers were collected *via* lyophilization.

Characterization of Polymers. *Molecular Weight Determination and Confirmation of Polymer Compositions.* Absolute molecular weights and polydispersities (M_w/M_n, PDI) of all polymers were determined by gel permeation chromatography (1200 Series, Shimadzu Technologies, Santa Clara, CA, USA) equipped with a miniDAWN TREOS, multiangle light scattering instrument (Wyatt Technologies, Santa Barbara, CA, USA) and a refractive index detector (Shimadzu Technologies) [columns: TSK Gel Super H−H guard; TSK Gel HM-N for gel separation, Tosoh Bioscience, Montgomeryville, PA, USA]. HPLC-grade DMF containing 0.05 M LiBr at 60 °C was used as the mobile phase at a flow rate of 0.35 mL/min. Absolute molecular weights were determined using reported d*n*/d*c* values for p(DMAEMA) (0.06 mL/g)[77−79] and PEG (0.13 mL/g).[80] Block copolymers that included pH-responsive blocks ((p(DMAEMA-*co*-BMA-*co*-PAA)) were analyzed *via* ^{1}H NMR spectroscopy (Bruker Avance 400) to confirm second-block composition, as previously described.[29]

Formation and Characterization of Nanoparticles. Size, polydispersity indices (PDI), and zeta (ζ) potentials of nanoparticles of p(DMAEMA)-*b*-p(DMAEMA-*co*-BMA-*co*-PAA), p(PEGMA)-*b*-p(DMAEMA-*co*-BMA-*co*-PAA), and p(DMAEMA)-*b*-p(BMA) were measured using a Zetasizer (Malvern Instruments, UK). The measurements were performed at 0.2 and 2.7 mg/mL for size measurements. ζ-Potentials were measured at 0.2 mg/mL and pH 7.2, except for p(DMAEMA)-*b*-p(DMAEMA-*co*-BMA-*co*-PAA), where ζ-potentials were measured at a range of pH (3.4−10.5), to correlate surface charges of particles to binding of mimetic dental surfaces.

Critical Micelle Concentrations of Nanoparticles. CMC of micelle-based nanoparticles composed of p(DMAEMA)-*b*-p(DMAEMA-*co*-BMA-*co*-PAA) was approximated using solvatochromic shifts in fluorescence emission of PRODAN (Molecular Probes, Eugene, OR, USA).[81,82] Briefly, PRODAN dissolved in methanol was aliquoted into black 96-well plates. After drying overnight, micelle solutions at a range of concentrations (0−2 mg/mL) were added and incubated overnight to achieve final PRODAN concentrations of 5.45×10^{-4} mg/mL. PRODAN emission was measured at two wavelengths (Ex/Em_1: 360 nm/436 nm and Ex/Em_2: 360 nm/518 nm), which correspond to emission of PRODAN in hydrophobic and hydrophilic phases, respectively. The ratio of emissions (hydrophobic phase/hydrophilic phase, Em_1/Em_2) was plotted *versus* log(micelle concentration), and CMC was determined as the concentration at which the emission ratio begins to increase with polymer concentration (Supplemental Figure S1).

Adsorption of Polymers onto Hydroxyapatite, Experimental Pellicle, and EPS Surfaces. *Preparation of Mimetic Dental Surfaces.* Three distinct surfaces were prepared to assess polymer binding properties: uncoated hydroxyapatite, hydroxyapatite coated with saliva (to mimic salivary pellicle), and glucan-coated sHA (to emulate EPS). Hydroxyapatite (CHT, BioRad) beads were washed twice with buffer (50 mM KCl, 1 mM KPO_4, 1 mM $CaCl_2$, 1 mM $MgCl_2$, 0.1 mM PMSF, and 0.02% NaN_3, in dd-H_2O, pH 6.5). Washed HA beads were incubated with whole human saliva to obtain saliva-coated hydroxyapatite.[4,49,57] gsHA surfaces were produced by incubating sHA beads with purified *S. mutans*-derived GtfB enzyme and sucrose in the presence of Alexa Fluor 647-labeled dextran (Ex/Em: 647 nm/668 nm) (Life Technologies) as described elsewhere.[81,82] Briefly, sHA beads were exposed to saturating amounts of GtfB (25 μg/mL) and incubated with sucrose (100 mM containing 1 μM Alexa Fluor 647, final concentration) at 37 °C for 4 h to allow glucans formation on the surface,[49,83] confirmed by confocal laser scanning microscopy (FV1000 Olympus, USA).[83]

Assessment of Polymer Binding. Quantitative assessment of polymer adsorption to dental surfaces was performed in triplicate by incubation of 1 μM Texas Red-labeled polymers in PBS with dental surfaces for 1 h at 37 °C. Note that the PBS used throughout this work was the following composition: 2.67 mM potassium chloride, 1.47 mM potassium phosphate monobasic, 137.9 mM sodium chloride, and 8.06 mM sodium phosphate dibasic, pH 7.2. The amount of adsorbed polymer was analyzed based on the difference in Texas Red signal (Ex/Em: 550 nm/617 nm) before and after adsorption, as measured by an Infinite N200 PRO microplate reader (Tecan, Switzerland). Results were confirmed by confocal laser scanning microscopy imaging of HA, sHA, and gsHA surfaces that were incubated with 85 μM polymer solutions for 1 h at 37 °C. Confocal images were analyzed for surface area coverage by polymers using ImageJ software (v. 1.47). Briefly, the images were transformed to 8 Bit, and built-in thresholds ("Moments") were applied to standardize the images. Five independent areas on each standardized image were selected for analysis. Binding of nanoparticles and p(DMAEMA) to hydroxyapatite at a range of pH (3.4−10.5) was also quantified to examine how protonation of the p(DMAEMA) tertiary amine residues affects adsorption.

Equilibrium Adsorption Curves. Adsorption of nanoparticles to HA, sHA, and gsHA was further analyzed at polymer concentrations of 0−15 μM in PBS. Langmuir equilibrium curves were fit to adsorption equilibrium data by GraphPad Prism software (v.6.03). From the fits, adsorption affinity constants (K_a [L-mmol^{-1}]) and maximal amounts of adsorbed nanoparticles to the various mimetics of dental surfaces (b_{max} [mmol/m^2]) were calculated. Nanoparticle adsorption was expressed relative to a surface area of hydroxyapatite beads, which was calculated according to the average diameter and density of the beads as provided by the manufacturer (80 μm and 0.63 g/ml, respectively).

Loading and Release of Antibiofilm Agent, Farnesol, from Micelles. *Drug Loading.* Micelles were loaded with farnesol by sonication similar to Tang *et al.*[84] Briefly, farnesol emulsions at a range of concentrations (0.2−1.5 mg/mL) were prepared by sonication (Sonic Raptor 250, Omni International, Kennesaw, GA, USA) in ddH_2O at 40% power. Emulsions were then mixed with 2.7 mg/mL of p(DMAEMA)-*b*-p(DMAEMA-*co*-BMA-*co*-PAA) micelles in glass scintillation vials. These solutions were placed in a bath sonicator (50 HT, VWR) for 5 min until the solutions were clear. Next the amounts of farnesol loaded were measured, and loading capacities ($100 \times (Wt_{loaded}/Wt_{micelle} + Wt_{loaded})$) and efficiencies ($100 \times (Wt_{loaded}/Wt_0)$) were calculated, where Wt_{loaded} is the amount of loaded drug, $Wt_{micelle}$ is the amount of micelle, and Wt_0 is the initial amount of farnesol in the emulsion.

Farnesol loading was measured by high-pressure liquid chromatography (HPLC). Briefly, nanoparticles loaded with farnesol were concentrated with 3 kDa centrifugal filter units (Amicon Ultra 0.5 mL, Millipore, USA). Nanoparticle retentate was removed, and filters were washed two additional times by centrifugation in 60% methanol in ddH_2O solutions to ensure complete recovery of free filtered farnesol. The change in the amount of farnesol in washes relative to measured initial farnesol concentration was calculated to determine loading capacity using HPLC (Shimadzu Technologies) with a C_{18} column (Kromasil Eternity, 4.6 mm × 50 mm, Supelco, Bellefonte, PA, USA), at flow rate of 0.5 mL/min, with a gradient of 10% to 90% of MeOH/H_2O over 20 min, and detection by UV absorbance (210 nm).

Nanoparticle sizes both before and after farnesol loading were examined using transmission electron microscopy.

Briefly, micelles were loaded with farnesol at loading capacities of 0 and 22 wt %, transferred to carbon-coated nickel grids, and dried for 2−5 min in the presence of 2% (w/v) phosphotungstic acid as a contrast agent. The images of free and loaded nanoparticles were taken at magnifications of 200 000× using a Hitachi 7650 transmission electron microscope (Hitachi, Schaumburg, IL, USA), attached to an 11 megapixel Erlangshen digital camera system (Gatan, Pleasanton, CA, USA).

Measuring Farnesol Release from Nanoparticles. Farnesol release from loaded micelles was quantified using dialysis. Briefly, farnesol loading was performed at *a priori* identified optimized loading efficacy (15 wt %) in Dulbecco's PBS. Drug-loaded micelles were placed in Dulbecco's PBS at pH 4.5 or 7.2 and dialyzed at 37 °C through 6−8 kDa dialysis membranes (Spectra/Por, Spectrum Laboratories), with daily changes of medium. Farnesol was quantified at day 0, 1, 2, 3, 4, and 7 by HPLC as previously detailed. At no time point was the concentration of free farnesol higher than its estimated solubility limit of 1.7 mg/L (US EPA; Estimation Program Interface (EPI) Suite V.3.12). Fits of the release data were performed assuming first-order release kinetics using GraphPad Prism software (v.6.03). According to the fits, release rate constants, k_r, and release half-times, $t_{1/2}$, were calculated according to the first-order release equation (% release = $100 \times (1 - e^{-k_{obs}*t})$), where percent release is the percent of drug released at time t, and k_{obs} is the observed kinetic constant of drug release, which was converted to release half-time according to the following relationship: $t_{1/2} = \ln(2)/K_{obs}$. Once the fit parameters were determined, first derivatives of the fit equations (release rate = d(% released)/$dt = 100 \times k_{obs}\, e^{-K_{obs}*t}$) were calculated to assess farnesol release rate over time.

Antibacterial Activity of Farnesol-Loaded Nanoparticles. Bioactivity of farnesol released from nanoparticles was demonstrated on planktonic *S. mutans* cells as described previously.[68] *S. mutans* UA159 (ATCC 700610; serotype c, as a model of biofilm-forming and cariogenic organism) cells were grown to mid-exponential phase in ultrafiltered (10 kDa membranes) tryptone-yeast extract broth (UFTYE, pH 7.0) containing 1% (w/v) glucose (at 37 °C; 5% CO_2) and harvested by centrifugation (5500*g*, 10 min, 4 °C). The cells were then washed three times with 0.89% NaCl and collected *via* centrifugation (5500*g*, 10 min, 4 °C). Cell suspensions were sonicated using a Branson Sonifier 450 (four 10 s pulses with 5 s intervals at 20 W; Branson Ultrasonics Co., CT, USA) to obtain single-celled suspensions as verified by light microscopy. The optical densities (600 nm) of cell preparations were adjusted to 0.5 ± 0.05, which corresponds to 1.5×10^9 *S. mutans* CFU/mL. Next, cell suspensions were centrifuged and resuspended in 1 mL of treatment solutions (1.5 mg/mL of free nanoparticles and farnesol-loaded nanoparticles (loaded with 0.3 mg/mL farnesol) and PBS). The samples were incubated with treatments for 1 h at 37 °C. Incubation solutions were diluted 10-fold and plated onto blood agar plates for CFU counts. CFU counts were performed directly after incubation and after three washes with PBS to ensure that the washing steps did not interfere with CFU counts. The plates were incubated for 48 h (37 °C, 5% CO_2) prior to visually counting CFUs.

Antibiofilm Activity of Nanoparticle-Mediated Farnesol Delivery. Streptococcus mutans UA159, a well-characterized EPS matrix producing and cariogenic pathogen,[4] was used to assess the effect of nanoparticle-mediated delivery of farnesol on biofilm formation and mechanical stability. Five treatment solutions were used to treat biofilms: free nanoparticles (1.5 mg/mL in PBS, pH 7.0), farnesol-loaded nanoparticles (1.5 mg/mL loaded with 0.3 mg/mL farnesol, in PBS, pH 7.0), free farnesol (0.3 mg/mL farnesol, in PBS, pH 7.0, 15% ethanol (EtOH)), vehicle control for free farnesol (PBS, pH 7.0, 15% EtOH), and PBS (pH 7.0). A 15% v/v ethanol solution was used as a vehicle to solubilize free farnesol, which is otherwise insoluble in aqueous media.[66] Biofilms of *S. mutans* UA159 were formed on saliva-coated hydroxyapatite surfaces (12.7 mm in diameter, 1 mm in thickness, Clarkson Chromatography Products Inc., South Williamsport, PA, USA) as detailed elsewhere.[85] The HA discs were placed vertically using a custom-made holder and grown in UFTYE (pH 7.0) with 1% sucrose at 37 °C and 5% CO_2. The sHA discs and biofilms were treated with the above-described solutions for 10 min, washed twice with sterile saline (0.89% NaCl), and transferred to culture media. The first treatment was applied directly after salivary pellicle formation (sHA), and then treated disks were transferred to culture media containing *S. mutans* (10^5 CFU/mL). Biofilms were allowed to form on the discs without interruption for 6 h, at which point a second treatment was applied. The next day, biofilms were treated three times and the culture media was changed twice (Supplemental Figure S7). After 44 h, the amount of colony forming units per dry weight of biofilms and biofilm removal under shear stress were assessed. For CFU and dry weight assessment, biofilms were removed from sHA discs *via* sonication;[66,67] our sonication procedure does not kill bacterial cells, while providing optimum dispersal and maximum recoverable counts. Aliquots of biofilm suspension were serially diluted and plated onto blood agar plates, and after 48 h incubation, the colonies were visually counted. The remaining biofilm suspension was washed twice with ddH_2O, oven-dried (into preweighed foil boats) for 2 h, and weighed.

For biofilm mechanical stability assays, each of the treated biofilms (free nanoparticles, nanoparticles loaded with farnesol, free farnesol, vehicle control, and PBS) was exposed to a constant shear stress of 0.184 N/m^2 for 10 min using a custom-built device that produces shear flow parallel to the biofilm surfaces[75] to induce disruption and detachment of the biofilm from the sHA surface. Shear stress at the biofilm surface was produced by flow generated by a rotating paddle and estimated as a function of Reynolds number of the flow (turbulent flow) and surface friction using the Blasius formula, as described in detail elsewhere.[75] A constant shear stress of 0.184 N/m^2 was applied directly to the biofilm surface, as such shear stress was previously determined as a threshold for initial removal of *S. mutans* biofilms from saliva-coated HA surfaces using our model.[75] After application of shear stress, the amount of biofilm dry weight (biomass) that remained on the sHA disc surface for each condition (free nanoparticles, nanoparticles loaded with farnesol, free farnesol, vehicle control for farnesol (15% v/v ethanol), and PBS) was determined, and biofilm removal data were expressed as fold change relative to PBS-treated biofilms. All experiments were performed in quadruplicates in three distinct experiments.

In Vivo Efficacy of Nanoparticle-Mediated Farnesol Delivery. Animal experiments were performed on a well-established model of dental caries disease as described elsewhere.[67,71] Briefly, Sprague−Dawley rats, 15 days old, were purchased with their dams from Harlan Laboratories (Madison, WI, USA) and screened for infection with *S. mutans*. Any animals infected with *S. mutans* prior to inoculation were removed from the study. Then, the animals were infected orally using an actively growing (mid-logarithmic) culture of *S. mutans* UA159, and their infection was checked *via* oral swabbing. Infected animals were randomly placed into four treatment groups of $n = 6$, and their teeth treated topically using a custom-made applicator twice daily. The treatment groups included (1) farnesol-loaded nanoparticles, (2) free nanoparticles, (3) free farnesol, and (4) vehicle for free farnesol (15% ethanol, v/v). Each group was provided the National Institutes of Health cariogenic diet 2000 and 5% sucrose water *ad libitum*. The experiment proceeded for 3 weeks; all animals were weighed weekly, and their physical appearance was noted daily. All animals gained weight equally among the experimental groups and remained in good health during the experimental period. At the end of the experimental period, animals were sacrificed, and teeth prepared for caries scoring according to Larson's modification of Keyes' system.[86] Determination of caries score of the codified jaws was performed by one calibrated examiner. This study was reviewed and approved by the University of Pennsylvania Institutional Animal Care and Use Committee (IACUC #805529).

Statistical Analysis. Significance among groups was assessed by two-way AVOVA followed by Tukey's tests for multiple comparisons at p-values of $p < 0.01$. Alternatively, a significance of Pearson correlations ($r^2 > 0$) that show trends in binding *versus* pH and ζ-potentials, as compared to no correlation ($r^2 = 0$), was assessed by two-tailed t tests at p-values of $p < 0.01$. Goodness of fits to first-order release kinetics and Langmuir

adsorption equilibrium were assessed by adjusted $R^2 > 0.98$ for all fits and D'Agostino & Pearson omnibus (K2) normality tests on residuals at p-values of $p < 0.05$. For *in vivo* analyses, t tests and the nonparametric Mann–Whitney test were utilized to test for the significance of farnesol-loaded nanoparticles *versus* nanoparticle control treatments and vehicle control for farnesol *versus* free farnesol, respectively, on the total number and severity of carious lesions with a significance level of $p < 0.05$.

Conflict of Interest: The authors declare no competing financial interest.

Acknowledgment. The authors gratefully acknowledge IADR/GlaxoSmithKline Innovation in Oral Care Awards (to M.I.K., D.B., H.K.), the National Science Foundation (BMAT DMR-1206219 (D.B.)), and the National Institutes of Health (K12ES019852 career development award to D.B., R01DE018023 to H.K., and R90DE022529 to M.I.K.) for funding this work. The authors thank James L. McGrath for access to the Malvern Zetasizer and TECAN microplate reader, Karen Bentley of URMC Electron Microscope Research Core for assistance with TEM imaging, and Dr. Linda Callahan of URMC Confocal and Conventional Microscopy Core for assistance with laser scanning microscopy. Y. Li, D. Kim, and H. Koo were involved in *in vivo* efficacy testing herein.

Supporting Information Available: Critical micelle concentration of nanoparticles (Figure S1); confirmation of nanoparticle attachment to *S. mutans* biofilm treated surfaces (Figure S2); nanoparticle loading at a range of drug concentrations (Figure S3); increase in nanoparticle size upon loading (Figure S4); nanoparticle release of farnesol in saliva-mimetic adsorption buffer (Figure S5); pH-responsive mechanisms of nanoparticle structure destabilization (Figure S6); treatment regimen during biofilm prevention assays (Figure S7). The material is available free of charge *via* the Internet at http://pubs.acs.org.

Note Added after ASAP Publication: This paper published ASAP on February 13, 2015. Corrections were made to maximal capacity and adsorption affinity amounts and Figure 2 was also replaced. The revised version was reposted on March 2, 2015.

REFERENCES AND NOTES

1. Davies, D. Understanding Biofilm Resistance to Antibacterial Agents. *Nat. Rev. Drug Discovery* **2003**, *2*, 114–122.
2. del Pozo, J. L.; Patel, R. The Challenge of Treating Biofilm-Associated Bacterial Infections. *Clin. Pharmacol. Ther.* **2007**, *82*, 204–209.
3. Flemmig, T. F.; Beikler, T. Control of Oral Biofilms. *Periodontol 2000* **2011**, *55*, 9–15.
4. Bowen, W. H.; Koo, H. Biology of Streptococcus mutans-Derived Glucosyltransferases: Role in Extracellular Matrix Formation of Cariogenic Biofilms. *Caries Res.* **2011**, *45*, 69–86.
5. Flemming, H. C.; Wingender, J. The Biofilm Matrix. *Nat. Rev. Microbiol.* **2010**, *8*, 623–633.
6. Marsh, P. D.; Moter, A.; Devine, D. A. Dental Plaque Biofilms: Communities, Conflict and Control. *Periodontol 2000* **2011**, *55*, 16–35.
7. Schlafer, S.; Raarup, M. K.; Meyer, R. L.; Sutherland, D. S.; Dige, I.; Nyengaard, J. R.; Nyvad, B. pH Landscapes in a Novel Five-Species Model of Early Dental Biofilm. *PLoS One* **2011**, *6*, e25299.
8. Xiao, J.; Klein, M. I.; Falsetta, M. L.; Lu, B.; Delahunty, C. M.; Yates, J. R., 3rd; Heydorn, A.; Koo, H. The Exopolysaccharide Matrix Modulates the Interaction between 3d Architecture and Virulence of a Mixed-Species Oral Biofilm. *PLoS Pathog.* **2012**, *8*, e1002623.
9. Koo, H.; Falsetta, M. L.; Klein, M. I. The Exopolysaccharide Matrix: A Virulence Determinant of Cariogenic Biofilm. *J. Dent. Res.* **2013**, *92*, 1065–1073.
10. Vroom, J. M.; De Grauw, K. J.; Gerritsen, H. C.; Bradshaw, D. J.; Marsh, P. D.; Watson, G. K.; Birmingham, J. J.; Allison, C. Depth Penetration and Detection of pH Gradients in Biofilms by Two-Photon Excitation Microscopy. *Appl. Environ. Microbiol.* **1999**, *65*, 3502–3511.
11. Bowen, W. H. The Stephan Curve Revisited. *Odontology* **2013**, *101*, 2–8.
12. Fejerskov, O.; Scheie, A. A.; Manji, F. The Effect of Sucrose on Plaque pH in the Primary and Permanent Dentition of Caries-Inactive and -Active Kenyan Children. *J. Dent. Res.* **1992**, *71*, 25–31.
13. Firestone, A. R.; Imfeld, T.; Schiffer, S.; Lutz, F. Measurement of Interdental Plaque pH in Humans with an Indwelling Glass pH Electrode Following a Sucrose Rinse: A Long-Term Retrospective Study. *Caries Res.* **1987**, *21*, 555–558.
14. Lingstrom, P.; Imfeld, T.; Birkhed, D. Comparison of Three Different Methods for Measurement of Plaque-pH in Humans after Consumption of Soft Bread and Potato Chips. *J. Dent. Res.* **1993**, *72*, 865–870.
15. Takahashi, N.; Nyvad, B. The Role of Bacteria in the Caries Process: Ecological Perspectives. *J. Dent. Res.* **2011**, *90*, 294–303.
16. Li, Y.; Burne, R. A. Regulation of the Gtfbc and Ftf Genes of Streptococcus mutans in Biofilms in Response to pH and Carbohydrate. *Microbiology* **2001**, *147*, 2841–2848.
17. Allaker, R. P. The Use of Nanoparticles to Control Oral Biofilm Formation. *J. Dent. Res.* **2010**, *89*, 1175–1186.
18. Cottenye, N.; Cui, Z. K.; Wilkinson, K. J.; Barbeau, J.; Lafleur, M. Interactions between Non-Phospholipid Liposomes Containing Cetylpyridinium Chloride and Biofilms of Streptococcus mutans: Modulation of the Adhesion and of the Biodistribution. *Biofouling* **2013**, *29*, 817–827.
19. Jones, M. N.; Francis, S. E.; Hutchinson, F. J.; Handley, P. S.; Lyle, I. G. Targeting and Delivery of Bactericide to Adsorbed Oral Bacteria by Use of Proteoliposomes. *Biochim. Biophys. Acta* **1993**, *1147*, 251–261.
20. Radovic-Moreno, A. F.; Lu, T. K.; Puscasu, V. A.; Yoon, C. J.; Langer, R.; Farokhzad, O. C. Surface Charge-Switching Polymeric Nanoparticles for Bacterial Cell Wall-Targeted Delivery of Antibiotics. *ACS Nano* **2012**, *6*, 4279–4287.
21. Chen, F.; Jia, Z. S.; Rice, K. C.; Reinhardt, R. A.; Bayles, K. W.; Wang, D. The Development of Dentotropic Micelles with Biodegradable Tooth-Binding Moieties. *Pharm. Res.* **2013**, *30*, 2808–2817.
22. Chen, F.; Liu, X. M.; Rice, K. C.; Li, X.; Yu, F.; Reinhardt, R. A.; Bayles, K. W.; Wang, D. Tooth-Binding Micelles for Dental Caries Prevention. *Antimicrob. Agents Chemother.* **2009**, *53*, 4898–4902.
23. Chen, F.; Rice, K. C.; Liu, X. M.; Reinhardt, R. A.; Bayles, K. W.; Wang, D. Triclosan-Loaded Tooth-Binding Micelles for Prevention and Treatment of Dental Biofilm. *Pharm. Res.* **2010**, *27*, 2356–2364.
24. Jones, M. N. Use of Liposomes to Deliver Bactericides to Bacterial Biofilms. *Liposomes, Part E* **2005**, *391*, 211–228.
25. Robinson, A. M.; Creeth, J. E.; Jones, M. N. The Use of Immunoliposomes for Specific Delivery of Antimicrobial Agents to Oral Bacteria Immobilized on Polystyrene. *J. Biomater. Sci., Polym. Ed.* **2000**, *11*, 1381–1393.
26. Benoit, D. S.; Boutin, M. E. Controlling Mesenchymal Stem Cell Gene Expression Using Polymer-Mediated Delivery of SiRNA. *Biomacromolecules* **2012**, *13*, 3841–3849.
27. Benoit, D. S. W.; Henry, S. M.; Shubin, A. D.; Hoffman, A. S.; Stayton, P. S. pH-Responsive Polymeric Sirna Carriers Sensitize Multidrug Resistant Ovarian Cancer Cells to Doxorubicin via Knockdown of Polo-Like Kinase 1. *Mol. Pharmaceutics* **2010**, *7*, 442–455.
28. Benoit, D. S. W.; Srinivasan, S.; Shubin, A. D.; Stayton, P. S. Synthesis of Folate-Functionalized RAFT Polymers for Targeted SiRNA Delivery. *Biomacromolecules* **2011**, *12*, 2708–2714.
29. Convertine, A. J.; Benoit, D. S. W.; Duvall, C. L.; Hoffman, A. S.; Stayton, P. S. Development of a Novel Endosomolytic Diblock Copolymer for SiRNA Delivery. *J. Controlled Release* **2009**, *133*, 221–229.
30. Gillies, E. R.; Frechet, J. M. J. pH-Responsive Copolymer Assemblies for Controlled Release of Doxorubicin. *Bioconjugate Chem.* **2005**, *16*, 361–368.
31. Tang, R. P.; Ji, W. H.; Panus, D.; Palumbo, R. N.; Wang, C. Block Copolymer Micelles with Acid-Labile Ortho Ester

Side-Chains: Synthesis, Characterization, and Enhanced Drug Delivery to Human Glioma Cells. *J. Controlled Release* **2011**, *151*, 18–27.
32. Fan, J. Q.; Zeng, F.; Wu, S. Z.; Wang, X. D. Polymer Micelle with pH-Triggered Hydrophobic-Hydrophilic Transition and De-Cross-Linking Process in the Core and Its Application for Targeted Anticancer Drug Delivery. *Biomacromolecules* **2012**, *13*, 4126–4137.
33. Wang, H.; Rempel, G. L. pH-Responsive Polymer Core-Shell Nanospheres for Drug Delivery. *J. Polym. Sci., Part A: Polym. Chem.* **2013**, *51*, 4440–4450.
34. Brahim, S.; Narinesingh, D.; Guiseppi-Elie, A. Release Characteristics of Novel pH-Sensitive P(HEMA-DMAEMA) Hydrogels Containing 3-(Trimethoxy-Silyl) Propyl Methacrylate. *Biomacromolecules* **2003**, *4*, 1224–1231.
35. Yildiz, B.; Isik, B.; Kis, M.; Birgul, O. pH-Sensitive Dimethylaminoethyl Methacrylate (DMAEMA)/Acrylamide (AAM) Hydrogels: Synthesis and Adsorption from Uranyl Acetate Solutions. *J. Appl. Polym. Sci.* **2003**, *88*, 2028–2031.
36. Kim, B. S.; Park, S. W.; Hammond, P. T. Hydrogen-Bonding Layer-by-Layer Assembled Biodegradable Polymeric Micelles as Drug Delivery Vehicles from Surfaces. *ACS Nano* **2008**, *2*, 386–392.
37. Ta, T.; Convertine, A. J.; Reyes, C. R.; Stayton, P. S.; Porter, T. M. Thermosensitive Liposomes Modified with Poly(N-Isopropylacrylamide-co-Propylacrylic Acid) Copolymers for Triggered Release of Doxorubicin. *Biomacromolecules* **2010**, *11*, 1915–1920.
38. Yin, X.; Hoffman, A. S.; Stayton, P. S. Poly(N-Isopropylacrylamide-co-Propylacrylic Acid) Copolymers That Respond Sharply to Temperature and pH. *Biomacromolecules* **2006**, *7*, 1381–1385.
39. Han, X.; Zhang, X. X.; Zhu, H. F.; Yin, Q. Y.; Liu, H. L.; Hu, Y. Effect of Composition of PDMAEMA-B-PAA Block Copolymers on Their pH- and Temperature-Responsive Behaviors. *Langmuir* **2013**, *29*, 1024–1034.
40. Li, H.; Miteva, M.; Kirkbride, K. C.; Cheng, M. J.; Nelson, C. E.; Simpson, E. M.; Gupta, M. K.; Duvall, C. L.; Giorgio, T. D. Dual Mmp7-Proximity-Activated and Folate Receptor-Targeted Nanoparticles for SiRNA Delivery. *Biomacromolecules* **2014**, *16*, 192–201.
41. Convertine, A. J.; Diab, C.; Prieve, M.; Paschal, A.; Hoffman, A. S.; Johnson, P. H.; Stayton, P. S. pH-Responsive Polymeric Micelle Carriers for Sirna Drugs. *Biomacromolecules* **2010**, *11*, 2904–2911.
42. Douroumis, D.; Fahr, A. *Drug Delivery Strategies for Poorly Water-Soluble Drugs*; John Wiley & Sons: New York, 2012.
43. van de Wetering, P.; Moret, E. E.; Schuurmans-Nieuwenbroek, N. M.; van Steenbergen, M. J.; Hennink, W. E. Structure-Activity Relationships of Water-Soluble Cationic Methacrylate/Methacrylamide Polymers for Nonviral Gene Delivery. *Bioconjugate Chem.* **1999**, *10*, 589–597.
44. van de Wetering, P.; Zuidam, N. J.; van Steenbergen, M. J.; van der Houwen, O. A. G. J.; Underberg, W. J. M.; Hennink, W. E. A Mechanistic Study of the Hydrolytic Stability of Poly(2-(Dimethylamino)Ethyl Methacrylate). *Macromolecules* **1998**, *31*, 8063–8068.
45. Bhat, R. R.; Tomlinson, M. R.; Genzer, J. Assembly of Nanoparticles Using Surface-Grafted Orthogonal Polymer Gradients. *Macromol. Rapid Commun.* **2004**, *25*, 270–274.
46. Sakai, K.; Smith, E. G.; Webber, G. B.; Baker, M.; Wanless, E. J.; Butun, V.; Armes, S. P.; Biggs, S. pH-Responsive Behavior of Selectively Quaternized Diblock Copolymers Adsorbed at the Silica/Aqueous Solution Interface. *J. Colloid Interface Sci.* **2007**, *314*, 381–388.
47. Lendenmann, U.; Grogan, J.; Oppenheim, F. G. Saliva and Dental Pellicle--a Review. *Adv. Dent. Res.* **2000**, *14*, 22–28.
48. Nobbs, A. H.; Lamont, R. J.; Jenkinson, H. F. Streptococcus Adherence and Colonization. *Microbiol. Mol. Biol. Rev.* **2009**, *73*, 407–450.
49. Schilling, K. M.; Bowen, W. H. Glucans Synthesized in Situ in Experimental Salivary Pellicle Function as Specific Binding Sites for Streptococcus mutans. *Infect. Immun.* **1992**, *60*, 284–295.
50. Gorbunoff, M. J.; Timasheff, S. N. The Interaction of Proteins with Hydroxyapatite 0.3. Mechanism. *Anal. Biochem.* **1984**, *136*, 440–445.
51. Miyake, N.; Sato, T.; Maki, Y. Effect of Zeta Potentials on Bovine Serum Albumin Adsorption to Hydroxyapatite Surfaces. *Bull. Tokyo Dent. Coll.* **2013**, *54*, 97–101.
52. Olsson, J.; Glantz, P. O. Effect of pH and Counter Ions on the Zeta-Potential of Oral Streptococci. *Arch. Oral Biol.* **1977**, *22*, 461–466.
53. Reynolds, E. C.; Wong, A. Effect of Adsorbed Protein on Hydroxyapatite Zeta Potential and Streptococcus mutans Adherence. *Infect. Immun.* **1983**, *39*, 1285–1290.
54. Weerkamp, A. H.; Uyen, H. M.; Busscher, H. J. Effect of Zeta Potential and Surface Energy on Bacterial Adhesion to Uncoated and Saliva-Coated Human Enamel and Dentin. *J. Dent. Res.* **1988**, *67*, 1483–1487.
55. Wilson, W. W.; Wade, M. M.; Holman, S. C.; Champlin, F. R. Status of Methods for Assessing Bacterial Cell Surface Charge Properties Based on Zeta Potential Measurements. *J. Microbiol. Methods* **2001**, *43*, 153–164.
56. Young, A.; Smistad, G.; Karlsen, J.; Rolla, G.; Rykke, M. Zeta Potentials of Human Enamel and Hydroxyapatite as Measured by the Coulter Delsa 440. *Adv. Dent Res.* **1997**, *11*, 560–565.
57. Ambatipudi, K. S.; Hagen, F. K.; Delahunty, C. M.; Han, X.; Shafi, R.; Hryhorenko, J.; Gregoire, S.; Marquis, R. E.; Melvin, J. E.; Koo, H.; *et al*. Human Common Salivary Protein 1 (Csp-1) Promotes Binding of Streptococcus mutans to Experimental Salivary Pellicle and Glucans Formed on Hydroxyapatite Surface. *J. Proteome Res.* **2010**, *9*, 6605–6614.
58. Al-Kattan, A.; Errassifi, F.; Sautereau, A. M.; Sarda, S.; Dufour, P.; Barroug, A.; Dos Santos, I.; Combes, C.; Grossin, D.; Rey, C.; *et al*. Medical Potentialities of Biomimetic Apatites through Adsorption, Ionic Substitution, and Mineral/Organic Associations: Three Illustrative Examples. *Adv. Eng. Mater.* **2010**, *12*, B224–B233.
59. Claessens, R. A. M. J.; Kolar, Z. I. Affinity of Tin(II) and Tin(II) Diphosphonates for Hydroxyapatite: An Experimental and Model Study. *Langmuir* **2000**, *16*, 1360–1367.
60. Leu, C. T.; Luegmayr, E.; Freedman, L. P.; Rodan, G. A.; Reszka, A. A. Relative Binding Affinities of Bisphosphonates for Human Bone and Relationship to Antiresorptive Efficacy. *Bone* **2006**, *38*, 628–636.
61. Pascaud, P.; Bareille, R.; Bourget, C.; Amedee, J.; Rey, C.; Sarda, S. Interaction between a Bisphosphonate, Tiludronate and Nanocrystalline Apatite: In Vitro Viability and Proliferation of Hop and HBMSC Cells. *Biomed. Mater.* **2012**, 7.
62. Sato, M.; Grasser, W.; Endo, N.; Akins, R.; Simmons, H.; Thompson, D. D.; Golub, E.; Rodan, G. A. Bisphosphonate Action - Alendronate Localization in Rat Bone and Effects on Osteoclast Ultrastructure. *J. Clin. Invest.* **1991**, *88*, 2095–2105.
63. Henneman, Z. J.; Nancollas, G. H.; Ebetino, F. H.; Russell, R. G. G.; Phipps, R. J. Bisphosphonate Binding Affinity as Assessed by Inhibition of Carbonated Apatite Dissolution in Vitro. *J. Biomed. Mater. Res., Part A* **2008**, *85A*, 993–1000.
64. Nancollas, G. H.; Tang, R.; Phipps, R. J.; Henneman, Z.; Gulde, S.; Wu, W.; Mangood, A.; Russell, R. G. G.; Ebetino, F. H. Novel Insights into Actions of Bisphosphonates on Bone: Differences in Interactions with Hydroxyapatite. *Bone* **2006**, *38*, 617–627.
65. Weiger, M. C.; Park, J. J.; Roy, M. D.; Stafford, C. M.; Karim, A.; Becker, M. L. Quantification of the Binding Affinity of a Specific Hydroxyapatite Binding Peptide. *Biomaterials* **2010**, *31*, 2955–2963.
66. Koo, H.; Hayacibara, M. F.; Schobel, B. D.; Cury, J. A.; Rosalen, P. L.; Park, Y. K.; Vacca-Smith, A. M.; Bowen, W. H. Inhibition of Streptococcus mutans Biofilm Accumulation and Polysaccharide Production by Apigenin and Tt-Farnesol. *J. Antimicrob. Chemother.* **2003**, *52*, 782–789.
67. Koo, H.; Schobel, B.; Scott-Anne, K.; Watson, G.; Bowen, W. H.; Cury, J. A.; Rosalen, P. L.; Park, Y. K. Apigenin and Tt-Farnesol with Fluoride Effects on S. mutans Biofilms and Dental Caries. *J. Dent. Res.* **2005**, *84*, 1016–1020.

68. Koo, H.; Rosalen, P. L.; Cury, J. A.; Park, Y. K.; Bowen, W. H. Effects of Compounds Found in Propolis on Streptococcus mutans Growth and on Glucosyltransferase Activity. *Antimicrob. Agents Chemother.* **2002**, *46*, 1302–1309.
69. Zhu, Z. X. Effects of Amphiphilic Diblock Copolymer on Drug Nanoparticle Formation and Stability. *Biomaterials* **2013**, *34*, 10238–10248.
70. Baranello, M. P.; Bauer, L.; Benoit, D. S. Poly(Styrene-Alt-Maleic Anhydride)-Based Diblock Copolymer Micelles Exhibit Versatile Hydrophobic Drug Loading, Drug-Dependent Release, and Internalization by Multidrug Resistant Ovarian Cancer Cells. *Biomacromolecules* **2014**, *15*, 2629–2641.
71. Falsetta, M. L.; Klein, M. I.; Lemos, J. A.; Silva, B. B.; Agidi, S.; Scott-Anne, K. K.; Koo, H. Novel Antibiofilm Chemotherapy Targets Exopolysaccharide Synthesis and Stress Tolerance in Streptococcus mutans to Modulate Virulence Expression in Vivo. *Antimicrob. Agents Chemother.* **2012**, *56*, 6201–6211.
72. Jabra-Rizk, M. A.; Meiller, T. F.; James, C. E.; Shirtliff, M. E. Effect of Farnesol on Staphylococcus aureus Biofilm Formation and Antimicrobial Susceptibility. *Antimicrob. Agents Chemother.* **2006**, *50*, 1463–1469.
73. Kaneko, M.; Togashi, N.; Hamashima, H.; Hirohara, M.; Inoue, Y. Effect of Farnesol on Mevalonate Pathway of Staphylococcus aureus. *J. Antibiot.* **2011**, *64*, 547–549.
74. Cross, S. E.; Kreth, J.; Zhu, L.; Qi, F. X.; Pelling, A. E.; Shi, W. Y.; Gimzewski, J. K. Atomic Force Microscopy Study of the Structure-Function Relationships of the Biofilm-Forming Bacterium Streptococcus mutans. *Nanotechnology* **2006**, *17*, S1–S7.
75. Hwang, G.; Klein, M. I.; Koo, H. Analysis of the Mechanical Stability and Surface Detachment of Mature Streptococcus mutans Biofilms by Applying a Range of External Shear Forces. *Biofouling* **2014**, *30*, 1079–1091.
76. Murthy, N.; Robichaud, J. R.; Tirrell, D. A.; Stayton, P. S.; Hoffman, A. S. The Design and Synthesis of Polymers for Eukaryotic Membrane Disruption. *J. Controlled Release* **1999**, *61*, 137–143.
77. Gallow, K. C.; Jhon, Y. K.; Genzer, J.; Loo, Y. L. Influence of Gradient Strength and Composition Profile on the Onset of the Cloud Point Transition in Hydroxyethyl Methacrylate/Dimethylaminoethyl Methacrylate Gradient Copolymers. *Polymer* **2012**, *53*, 1131–1137.
78. Kryuchkov, M. A.; Detrembleur, C.; Jerome, R.; Prud'homme, R. E.; Bazuin, C. G. Synthesis and Thermal Properties of Linear Amphiphilic Diblock Copolymers of L-Lactide and 2-Dimethylaminoethyl Methacrylate. *Macromolecules* **2011**, *44*, 5209–5217.
79. Vesterinen, A.; Lipponen, S.; Rich, J.; Seppala, J. Effect of Block Composition on Thermal Properties and Melt Viscosity of Poly[2-(Dimethylamino)Ethyl Methacrylate], Poly(Ethylene Oxide) and Poly(Propylene Oxide) Block Co-Polymers. *Express Polym. Lett.* **2011**, *5*, 754–765.
80. Liu, Y. G.; Lipowsky, R.; Dimova, R. Concentration Dependence of the Interfacial Tension for Aqueous Two-Phase Polymer Solutions of Dextran and Polyethylene Glycol. *Langmuir* **2012**, *28*, 3831–3839.
81. Adhikary, R.; Barnes, C. A.; Petrich, J. W. Solvation Dynamics of the Fluorescent Probe Prodan in Heterogeneous Environments: Contributions from the Locally Excited and Charge-Transferred States. *J. Phys. Chem. B* **2009**, *113*, 11999–12004.
82. Rodriguez, V. B.; Henry, S. M.; Hoffman, A. S.; Stayton, P. S.; Li, X. D.; Pun, S. H. Encapsulation and Stabilization of Indocyanine Green within Poly(Styrene-Alt-Maleic Anhydride) Block-Poly(Styrene) Micelles for near-Infrared Imaging. *J. Biomed. Opt.* **2008**, 13.
83. Klein, M. I.; Duarte, S.; Xiao, J.; Mitra, S.; Foster, T. H.; Koo, H. Structural and Molecular Basis of the Role of Starch and Sucrose in Streptococcus mutans Biofilm Development. *Appl. Environ. Microbiol.* **2009**, *75*, 837–841.
84. Tang, Y. Q.; Liu, S. Y.; Armes, S. P.; Billingham, N. C. Solubilization and Controlled Release of a Hydrophobic Drug Using Novel Micelle-Forming ABC Triblock Copolymers. *Biomacromolecules* **2003**, *4*, 1636–1645.
85. Koo, H.; Xiao, J.; Klein, M. I.; Jeon, J. G. Exopolysaccharides Produced by Streptococcus mutans Glucosyltransferases Modulate the Establishment of Microcolonies within Multispecies Biofilms. *J. Bacteriol.* **2010**, *192*, 3024–3032.
86. Larson, R. M. In *Merits and Modifications of Scoring Rat Dental Caries by Keyes' Method*; Symposium on Animal Models in Cariology; Washington, D.C., 1981; p 203.